Detection limits of CO_2 in fluid inclusions using microthermometry and Raman spectroscopy and the spectroscopic characterization of CO_2

by

Kevin Michael Rosso

Thesis submitted to the faculty of Virginia Polytechnic Institute and State University
in partial fulfillment of the requirements of the degree of

MASTER OF SCIENCE
in
GEOLOGICAL SCIENCES

APPROVED:

Robert J. Bodnar
Chairman

Michael F. Hochella, Jr.

Richard H. Zallen

October, 1994

Blacksburg, Virginia

DETECTION LIMITS OF CO_2 IN FLUID INCLUSIONS USING MICROTHERMOMETRY AND RAMAN SPECTROSCOPY AND THE SPECTROSCOPIC CHARACTERIZATION OF CO_2

by

Kevin Michael Rosso

Robert J. Bodnar, Chairman

Department of Geological Sciences

(ABSTRACT)

In many geologic environments, dominantly aqueous solutions contain low concentrations of CO_2. At ambient temperature, in fluid inclusions which trap these solutions, the typical phase assemblage consists of a CO_2-rich vapor (where $P_{CO_2} \approx P_{internal}$) and an aqueous phase containing dissolved salts and CO_2. In this study, the CO_2 minimum detection limits (MDLs) using microthermometry and laser Raman spectroscopy are established in terms of P_{CO_2} using synthetic H_2O-CO_2 inclusions. The purpose of the microthermometric experiments was to examine the diagnostic CO_2 phase changes and determine the quantity of CO_2 necessary to result in observable solid CO_2 melting. The results of these experiments show that an observable solid CO_2 melting event requires $P_{CO_2} \geq 45$ bar at 25°C.

The Raman spectroscopic detection limits were investigated using a multichannel Raman spectrometer. Because the Raman spectroscopic MDLs are a function of counts, the CO_2 MDLs were determined by collecting signal-to-noise ratios for both the upper and lower ν_1-$2\nu_2$ bands as a function of CO_2 pressure (5-60 bars) and over a range of integration times and incident laser power to predict the optimal instrument settings. The resulting CO_2 MDLs are on the order of 1 bar for our instrument.

The band splitting of the ν_1-$2\nu_2$ diad as a function of CO_2 pressure was measured up to 500 bar at ambient temperature. The CO_2 pressures were converted to ρ_{CO_2} and the results are given in terms of the frequency separation between the upper and lower bands. These results are compared to those of previous studies. An analysis of the estimated errors indicates that the technique can be used to determine CO_2 densities in fluid inclusions containing a homogenous, free CO_2 phase to a precision of approximately $\pm$ 0.02 g/cm^3.

The temperature dependence of the intensity ratio of the hot bands to the ν_1-$2\nu_2$ diad was measured from 270 to 315 K. The close agreement between the calculated and observed results indicate that laser induced sample heating is not significant. The intensity ratio can be used to estimate the CO_2 temperature and, combined with the Raman density determination, allows calculation of the CO_2 pressure.

Acknowledgments

I would like to thank the members of my committee, Bob Bodnar, Mike Hochella, and Dick Zallen for the insightful guidance and many contributions to the success of this work. Bob Bodnar and the Department of Energy are also thanked for the constant financial support during the first part of my graduate education which made presenting and completing this work possible. Many others contributed much to my education. Frank Harrison and Dan Smith helped greatly in the experimental and mechanical aspects. Udo Becker contributed much to my understanding of physics and taught me applied statistics. Jodi Junta taught me how to make an outstanding presentation both graphically and verbally. Scott Mutchler introduced me to a spectral treatment program which became essential to this study. Conversations with Christian Schmidt increased my knowledge of high temperature and pressure thermodynamic relationships in fluids. I also wish to thank I-Ming Chou at the U.S.G.S in Reston, Virginia for some essential supplies. Finally, none of this would have been possible without the loving support from my parents John and Lorna, my brother Ken, my sister Kelly, and my fiancee Jodi.

Table of Contents

List of Figures

Introduction

In many geological environments, aqueous solutions contain CO_2 as the volatile component. For example, fluid inclusions in epithermal precious metal deposits contain low salinity aqueous solutions with low concentrations of CO_2 (< 1 molal) (HEDENQUIST and HENLEY, 1985). At ambient temperature, the typical phase assemblage in these fluid inclusions consists of a CO_2-rich vapor phase and an aqueous phase containing dissolved NaCl and some dissolved CO_2 (BODNAR et al., 1985). Reconstruction the the parent fluid chemistry at the time of mineral formation requires that the bulk fluid composition be known. In order to accurately determine the bulk concentration of CO_2 in these inclusions, the salt concentration, phase ratios, internal pressure (usually attributed entirely to the partial pressure of CO_2), and phase ratios must be known. Techniques for determining salinities of these inclusions have been addressed recently by DIAMOND (1994a). ANDERSON and BODNAR (1993) and ROEDDER (1984) have discussed techniques for estimating phase ratios. The focus of this study is the determination of P_{CO_2}, which usually can be accomplished by estimating CO_2 densities and using an appropriate equation of state. This must involve characterization of individual CO_2 phases or the observation of the CO_2 homogenization temperature. The detection limits of CO_2 must also be evaluated to know how much CO_2 can be overlooked during analyses.

Using microthermometry, the detection of CO_2 and determination of P_{CO_2} is done by observing the behavior of phase changes at low temperatures. Unfortunately, during routine heating and cooling studies, low concentrations of CO_2 are not easily detected (SASADA, 1985; ULRICH and BODNAR, 1988). In addition, even more CO_2 is required to determine P_{CO_2} from the CO_2 homogenization temperature where liquid + vapor $\rightarrow$ vapor. The first part of this study investigates the microthermometric detection limits of CO_2.

The advantages of applying Raman spectroscopy to the analysis of geochemically relevant gases in fluid inclusions has been well known for some time. Also, experimental difficulties and instrumental complications are well discussed in previous studies (see PASTERIS et al., 1988; BURKE, 1994). However, many studies neglect discussion of the fundamentals of what is actually being measured for a particular Raman active species. This has led to interpretation problems, such as the misuse of CO_2 scattering cross sections in relative quantitative analyses (BURKE, 1994). Therefore, in this study we include a discussion of the fundamentals of the Raman spectrum of CO_2.

Compared to microthermometry, Raman spectroscopy provides an improved detection limit for gases such as CO_2 (WOPENKA and PASTERIS, 1987). Because Raman spectroscopic detection limits are a function of counts, the inherent counting efficiency of the particular instrument causes the results and precision to be instrument specific. In this study, we use a different instrument than that used by WOPENKA and PASTERIS to re-examine the CO_2 detection limits using optimized settings.

The Raman spectrum of CO_2 contains information which can be used to characterize CO_2 density and temperature. Several previous studies have documented density dependent band shifts in the spectrum of CO_2 (HOWARD-LOCK and STOICHEFF, 1971; WANG and WRIGHT, 1973; WRIGHT and WANG, 1973; BERTRAN, 1983; CHANDRASEKHARAN and GARRABOS, 1988; GARRABOS et al., 1980, 1989a, 1989b). These studies were directed at determining Fermi resonance parameters and band assignments for the ν_1-$2\nu_2$ Fermi diad. Although these papers show the same trends for CO_2 band shifts, there are discrepancies which preclude their usefulness in accurately determining CO_2 densities from band frequencies. In this study, we investigate the density dependence of frequency splitting in the ν_1-$2\nu_2$ Fermi diad.

In order to accurately calculate the internal pressure from Raman-based density determinations, the temperature in the excitation volume must be known. In many cases, it is not known whether the surrounding temperature of the sample agrees with the temperature in the excitation volume due to laser induced heating. Hot bands in the CO_2 spectrum provide an internal temperature check. In this study, we determine the temperature dependence of the intensity ratio of hot bands to the ν_1-$2\nu_2$ Fermi diad in the temperature range 270 to 315 K for use as a temperature indicator in conjunction with density measurements using CO_2 band splitting.

Experimental Procedure

Synthetic H_2O-CO_2 fluid inclusions were made using the procedure described by BODNAR and STERNER (1987) and STERNER and BODNAR (1991). Fluid compositions were 0.5, 1.0, 2.0, 5.0, and 10.0 mol% CO_2. Formation conditions were 500°C and 5 kbar, 600°C and 3 kbar, and 700°C and 1.5 kbar for each fluid composition. The samples were analyzed using a USGS-type heating/cooling stage mounted on a polarizing microscope equipped with a 40x ultra-long working distance objective lens. Inclusions selected for analysis ranged in size from 1 to 25 μm average diameter. To compare the microthermometric detection limit with that determined using laser Raman spectroscopy, the partial pressure of CO_2 ($P_{CO_2} \approx$ total internal pressure) at 25°C and bulk density was calculated for this suite of inclusions using the algorithm in BODNAR et al. (1985). The resultant internal pressure range was 5 - 64 bars.

The Raman detection limits for CO_2 and the density dependence of the band shifts were determined using a gas cell described in CHOU et al. (1990). The cell consists of a fused silica glass capillary tube with an external diameter of 3 mm and an internal diameter

of 1 mm. High pressure steel tubing connects the cell to a screw-piston pressure generator which is linked to the CO_2 source tank containing gaseous CO_2 of purity >99.98%. The internal pressure was measured using an industry calibrated pressure transducer. The entire system is capable of attaining a pressure of about 700 bars. The CO_2 spectra were collected at ambient temperature (approximately 22°C) and from 5 - 60 bars in gas phase CO_2 and from 70 - 500 bars in the liquid phase. The pressure and temperature were used to calculate density using the equations of state of DUSCHEK et al. (1990) in the low pressure range and BOTTINGA and RICHET (1981) in the high pressure range. Because the peak intensity is a function of counts, the spectra were collected over a range of integration time and laser power settings at each CO_2 pressure in order to determine settings which optimize the signal-to-noise ratio.

The intensity ratio of hot bands to Fermi diad bands was measured using a doubly terminated fused quartz capillary tube of pure CO_2 and a temperature controlled optical stage. Pure CO_2 was trapped in the capillary, 30 mm in length (3 mm O.D., 1 mm I.D.), by connecting its open end to the CO_2 source tank using high pressure tubing, epoxy cement, and a steel coupling. The system was evacuated, flushed with CO_2, and filled to tank pressure. Solid CO_2 crystals were formed by submerging the capillary end, wrapped in wet tissue, into liquid nitrogen. The cooled system was then evacuated leaving the crystals under low vacuum. The capillary was cut and fused using an oxygen-methane torch while the CO_2 bearing end was insulated by the exterior ice layer. After warming to ambient temperature, the density of the resulting trapped gas was determined using the relationship between ν_1-$2\nu_2$ diad band splitting and density. The estimated density in the capillary was 0.08 g/cm^3 at ambient temperature corresponding to an internal pressure of about 37 bars. The sample was loaded into a low vacuum (to 5 torr) cell containing a temperature controlling sample platform which is cooled by internally circulating nitrogen

and the Joule-Thompson effect. A schematic cross-section through the stage depicting the general setup is shown in Figure 1. The effective temperature range is 80 - 373 K and temperature control precision is 0.01 K. At each temperature, the sample was allowed 15 minutes to ensure thermal equilibrium according to manufacturer specifications. The density of the gas was monitored at each temperature using the ν_1-$2\nu_2$ band splitting. No deviation from 0.08 g/cm^3 was detected over the temperature range used, indicating isochoric behavior.

Raman spectra were obtained using a Dilor XY modular laser Raman spectrometer coupled with an Olympus BH2 optical microscope. An argon ion laser provided the excitation energy on the 514.5 nm line. The scattered light was analyzed using a 0.64 m focal-length foremonochromator in double subtractive mode and a multichannel spectrometer. The detector is a 256 by 1024 CCD Peltier-cooled array. Spectra were collected using a bandpass of 944.7 - 1805.1 cm^{-1} over 1024 pixels of the detector corresponding to 0.84 cm^{-1}/pixel. Detection limit and band shift spectra were collected using the following instrument settings: 300, 500, 750, 1000 mW set laser power, 60, 120, 180, 240 seconds integration time, entrance and exit slits set at 100 μm (4.6 cm^{-1} spectral width). Spectra pertaining to hot band intensities were collected using 200 mW, 240 seconds, and 200 μm slit widths (8.9 cm^{-1} spectral width). The spectrometer was regularly calibrated between sets of spectra using neon lines at 566.3 nm, 565.7 nm, 565.3 nm, 556.3 nm, 544.9 nm, and 543.4 nm (in air) (BURNS et al., 1950) and a mercury line at 546.1 nm in order to check the absolute wavenumber alignment and to correct for any frequency offset. This offset was found to be small and linear in all cases. Intensity calibration was done using a tungsten lamp (MALYJ and GRIFFITHS, 1983).

A 32x objective (numerical aperture = 0.30) was used for the above experiments. However, Raman analyses of fluid inclusions frequently utilize an ultra-long working

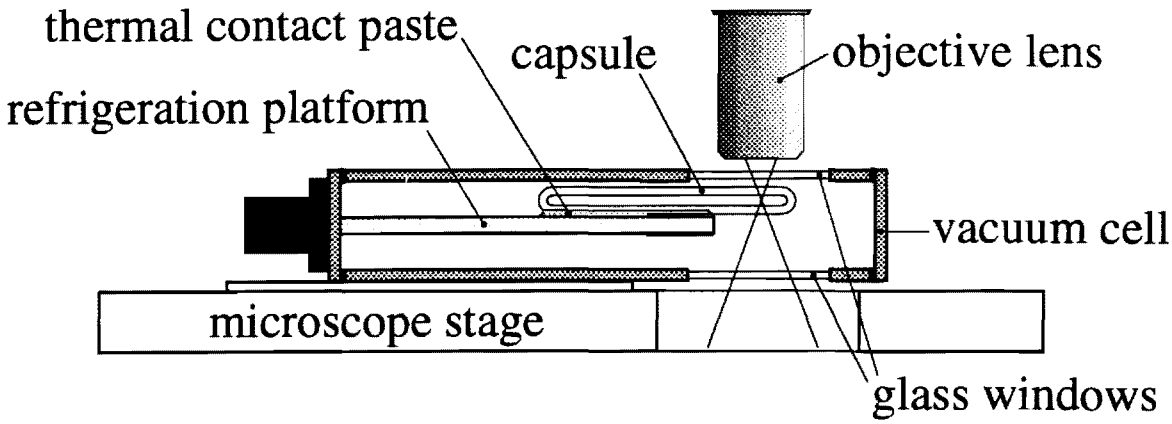

FIGURE 1: The analytical setup used to determine the intensity ratio of the hot band diad to the ν_1-$2\nu_2$ Fermi diad. The cell is kept under low vacuum (5 torr) to insulate the temperature controlling platform and the sample from thermal contact with the atmosphere. Minute conduits in the platform circulate gaseous N_2 which cools the sample utilizing the Joule-Thompson effect. A heating element, temperature sensor, and computer control serve to balance and stabilize the temperature to the setpoint. The sample is kept in thermal contact with the platform with contact paste. The optical working distance of the cell is $\geq$ 3 mm.

distance 80x objective (numerical aperture = 0.75). In order to relate their relative transmittivities, the laser power throughput of each objective lens was measured using a power meter. The transmitted power was measured at various laser power settings from 10 mW to 1.5 W and these experiments were repeated three times.

Spectra were analyzed using Spectra Calc™ version 2.2 software and a maximum likelihood fitting program in the Square Tools™ version 1.0 utility package. Individual CO_2 band shapes were least-squares fit (summed combination of Gaussian and Lorentzian peak shapes) to minimize errors and maximize precision in the determination of peak parameters. The optimized parameters are the peak position, peak height, full-width at half-maximum, and Lorentzian fraction.

Results / Discussion

MICROTHERMOMETRIC DETECTION OF CO_2

The CO_2 phase relationships of fluids relevant to this study can be approximated by the H_2O-CO_2 phase diagram (Figure 2) at low temperatures constructed from the data of LARSON (1955). Here, for simplicity, the phase boundaries are essentially that of pure CO_2 phases, with the H_2O liquidus and freezing point depression and the CO_2 clathrate stability field superimposed. For a detailed description of the H_2O-CO_2 binary system, the reader is referred to DIAMOND (1994b). During fluid inclusion analyses, after supercooling the sample, the behavior of phase changes that occur with increasing temperature is largely dependent on the temperature-pressure path within the inclusion. This path is a function of the bulk CO_2 concentration and the bulk density of the fluid. Both of these variables can be expressed in terms of the corresponding partial pressure of CO_2 (P_{CO_2}) in the inclusion at ambient temperature. The contribution of the partial

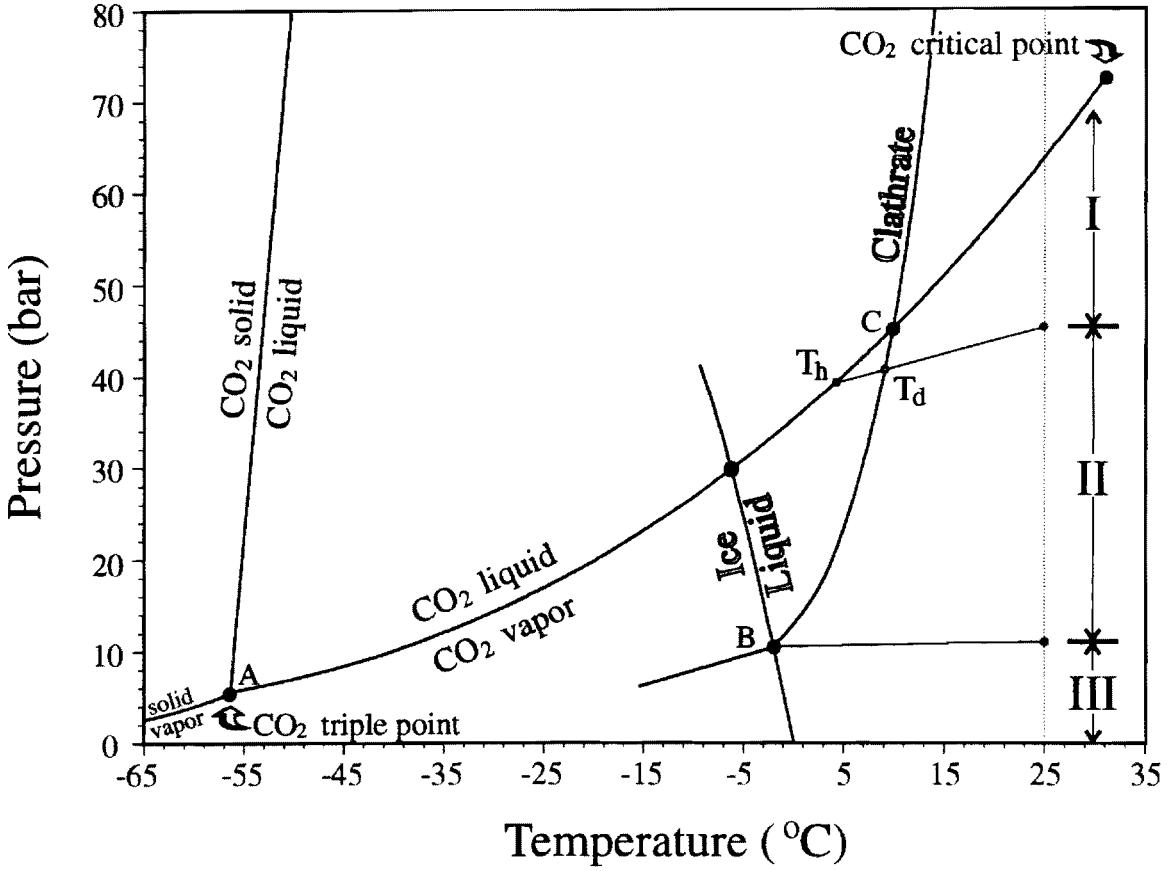

FIGURE 2: H_2O-CO_2 phase diagram modified from LARSON (1955). Point A is the CO_2 triple point (-56.6°C, 6 bars), invariant point B is where clathrate, ice, aqueous solution, and a vapor phase coexist (-1.48°C, 10.4 bars), and invariant point C is where clathrate, aqueous solution, liquid CO_2, and vapor are stable (10.0°C, 45 bars). Type II inclusions show only clathrate dissociation over the entire temperature range as an indicator of the presence of CO_2. Type III inclusions show no diagnostic CO_2 phase.

pressure of H_2O to the total internal pressure is negligible in the temperature range of this study. The diagnostic phase transitions which occur with increasing temperature can be categorized into three groups as shown in Figure 2:

I) High P_{CO_2}: Solid CO_2 melting is observed at the CO_2 triple point (point A at −56.6°C); clathrate dissociation is observed at temperatures ≥ T_d.

II) Medium P_{CO_2}: Solid CO_2 melting is not observable; clathrate dissociation is observed at temperatures between T_d and -1.48°C (point B on Fig. 2).

III) Low P_{CO_2}: Neither solid CO_2 melting nor clathrate dissociation are observed.

CO_2 is most easily detected in group I inclusions which either contain a liquid CO_2 phase at ambient temperature or have a relatively high CO_2 homogenization temperature of more than about 3°C (BODNAR et al., 1985). These inclusions will show a solid CO_2 melting event at -56.6°C and clathrate dissociation will occur near 10°C. Both of these transitions indicate the presence of CO_2. In group II inclusions, a discrete liquid CO_2 phase will not be observed at any temperature, however the dissociation temperature of clathrate can be observed and used as an indicator of the presence of CO_2. Group III inclusions will not display any phase change diagnostic of CO_2 during microthermometric analysis.

The boundary between groups II and III is defined by the temperature-pressure point where clathrate can be distinguished from ice crystals. Theoretically, this point is located at point D (-1.48°C, 10.4 bars) in Figure 2 which is the point of congruent ice melting and clathrate dissociation. At 25°C, the calculated internal pressure of the fluid which behaves in this manner is not significantly different from the pressure at -1.48°C. This means that for a fluid inclusion which has P_{CO_2} slightly greater than 10.4 bars at

25°C, clathrate dissociation will occur. However, in practice, observing clathrate dissociation is complicated by many factors such as inclusion size, shape, mineral and microscope optics, etc., and the individual contributions of these are not easily isolated. Also, the similarities between the refractive index of clathrate and that of aqueous solution make clathrate difficult to detect optically (ROEDDER, 1972). As a result, much higher amounts of CO_2 can be present in the inclusion and not be detectable by observing clathrate dissociation. However, clathrate can be detected to some extent by observing the shape and/or position of the vapor phase using temperature cycling near the point of clathrate dissociation (COLLINS, 1979; SASADA, 1985; DIAMOND, 1994b). Using this technique with ideal inclusions which are optically clear and regularly shaped, the detection limit of CO_2 based on clathrate dissociation is approximately 10.4 bars at 25°C (HEDENQUIST and HENLEY, 1985).

The amount of CO_2 that defines the boundary between inclusion groups I and II was estimated in this study. The distinction was based on whether a sample showed a reproducible solid CO_2 melting event. The "magnitude" of the solid CO_2 melting event is dominantly dependent on the amount of liquid CO_2 available to form solid CO_2 during cooling. This is, in turn, a function of the amount of "free" CO_2 remaining in the inclusion after the formation of clathrate. During cooling, the metastable nucleation of clathrate occurred at temperature well within the ice stability field for small inclusions (< 20 μm) analyzed in this study. The nucleation of the first solid phase, clathrate, thus provided a nucleation center for the next solid phase, ice. The effect is to have clathrate and ice forming at nearly identical times. The "double freezing" phenomenon described in COLLINS (1979), in which clathrate forms before ice even though it forms in the ice stability field, was not observed in this study. This is probably owing to the fact that his inclusions contained 8 to 14 wt. % NaCl in solution after the nucleation of clathrate. The

addition of salt lowers the activity of H_2O which depresses the freezing point and increases the ice nucleation barrier. Here, as clathrate and ice form simultaneously, they compete for free H_2O molecules unbound in a solid phase. This minimizes the amount of clathrate which is formed during cooling. Thus after clathrate and ice form, there is an apparent disequilibrium between clathrate, ice, and free CO_2. The important implication for repetitive analyses is that the cooling leg of the temperature cycle should be started from higher than 10°C in order to maximize the resulting amount of free CO_2 at low temperatures. During the warming leg, at the point of ice melting, the liberation of H_2O molecules from ice resolves the disequilibrium between the "free" CO_2 and the amount of clathrate. The volume of clathrate will increase as long as free CO_2 and H_2O are in chemical communication and the temperature and pressure are within the clathrate stability field.

Assuming the amount of CO_2 which is bound in the clathrate phase during cooling from temperatures higher than 10°C is essentially constant, the amount of free CO_2 available at low temperatures can be related to the homogenization temperature (T_h) of the free CO_2. This is the intersection point of the temperature-pressure path with the liquid-vapor curve (see Figure 2). Because the free CO_2 now behaves as a pure phase, the homogenization temperature is dependent on its density which is a function of both the starting bulk CO_2 concentration and bulk solution density. Inclusions containing low concentrations and/or having low densities will have low CO_2 homogenization (liquid + vapor $\rightarrow$ vapor) temperatures. Increasing CO_2 concentration and/or bulk density causes the CO_2 homogenization temperature to increase. Figure 3 shows densities of coexisting CO_2 liquid and vapor in the pure CO_2 system from the critical temperature (31.1°C) to the triple point (-56.6°C). For a given homogenization temperature, the proportions of CO_2 present in the form of liquid and vapor at -56.6°C are determined using the lever rule as

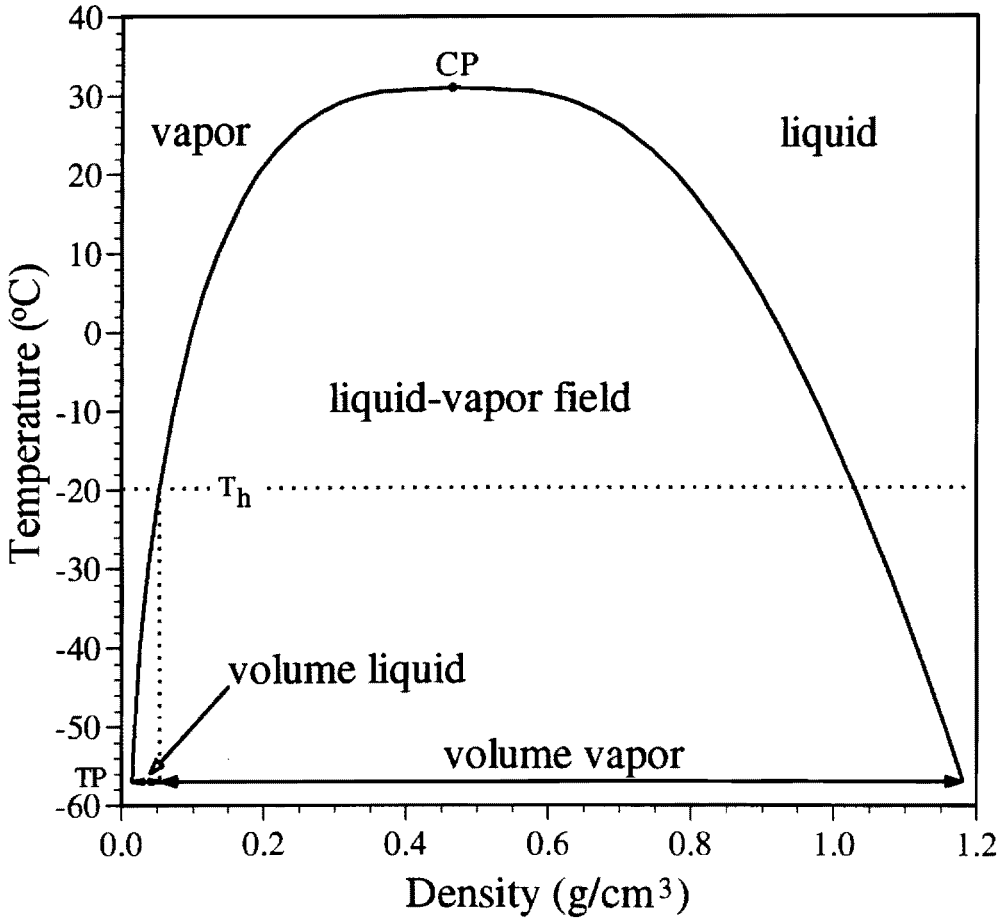

FIGURE 3: Pure CO_2 solvus from the triple point (-56.6°C) to the critical point (31.1°C) from data of LOWRY and ERICKSON (1927). For a given T_h, the volume proportions of liquid and vapor phases which are present at the triple point (TP) temperature can be determined using the lever rule as shown.

shown in Figure 3. This shows that, for inclusions which homogenize to the vapor phase, higher homogenization temperatures (and therefore higher CO_2 densities) result in a larger volume percent liquid CO_2 present at the triple point. This means that more CO_2 in the form of liquid will be available to form solid CO_2 and thus contribute to an observable solid CO_2 melting event during heating.

Due to the fact that the homogenization temperature is essentially proportional to the internal pressure at 25°C for the samples in this study, the detection limit of inclusion groups I and II can be represented by isobars in bulk density-composition space as shown in Figure 4. This shows the calculated bulk density and known bulk composition of the samples analyzed in this study. Also shown are calculated 25°C internal pressure isobars. The samples at points marked A (P_{CO_2} = 47 bars) and B (P_{CO_2} = 45 bars) were used to estimate the solid CO_2 melting detection limit isobar because the visible limit of a reproducible solid CO_2 melting event was documented in these samples. It was observed only in optically clear inclusions larger than 6 μm and the ratio of the visible area of solid CO_2 crystals to CO_2 vapor was small, approximately 0.05. Therefore we estimate the P_{CO_2} at 25°C necessary to observe solid CO_2 melting must be at least 45 bars. This is in agreement with the estimation of HEDENQUIST and HENLEY (1985) stating that P_{CO_2} ~ 45 bars is required to result in the condensation of a liquid CO_2 phase. This limit also represents the minimum amount of CO_2 required to use the CO_2 homogenization temperature as a means of estimating the density.

Figure 4 shows the boundaries between the fields of inclusion groups I, II, and III. The clathrate detection limit is shown in Figure 4 as the 10.4 bars isobar and the solid CO_2 detection limit is shown as the 45 bars isobar (solid lines). The region above the heavy solid line represents inclusions which contain a liquid CO_2 phase at 25°C. This region is included in the field marked I. Notice that when using clathrate dissociation as an

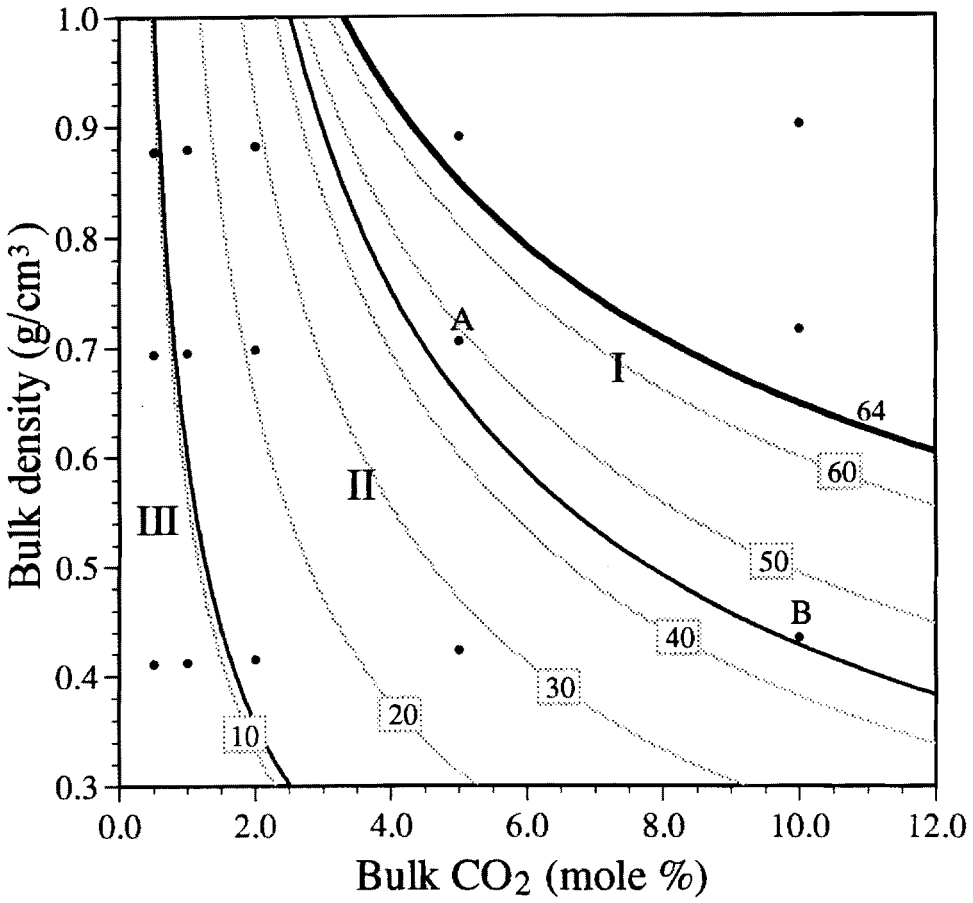

FIGURE 4: Calculated CO_2 density-composition plot using the algorithm in BODNAR et al. (1985). The points represent the samples in this study. The light lines are isobar contours for internal pressure at 25°C. Points to the high density/high concentration side of the heavy line marked 64 show both CO_2 liquid and vapor at 25°C. Points marked A and B are located near the solid CO_2 melting detection limit (solid line at 45 bars). Samples with internal pressures to the low density / low concentration side of this line do not show detectable solid CO_2 melting. The solid line at 10.4 bars represents the detection limit of clathrate dissociation. The inclusion types discussed in this study are labelled as regions I, II, and III.

indicator of CO_2, for low bulk densities, 2 mole % CO_2 in the bulk fluid might not be detected. Overall, microthermometry is not sensitive enough to detect small amounts of CO_2. In group I inclusions, where $P_{CO_2} < 10.4$ bars, CO_2 behaves as a dissolved species in the aqueous solution. The significance of detecting CO_2 in group III fluid inclusions is addressed in HEDENQUIST and HENLEY (1985).

RAMAN SPECTROSCOPY

The Spectrum of CO_2

The number of degrees of freedom for a molecule is 3N where N is the number of atoms. To isolate the vibrational degrees of freedom, three rotational degrees of freedom (about x, y, z) and three translational degrees of freedom (along x, y, z) must be subtracted, resulting in 3N – 6 vibrational degrees of freedom. For molecules having linear symmetry, rotation about that axis can be neglected, leaving 3N – 5 vibrational degrees of freedom. The CO_2 molecule is linear and thus has four modes of vibration, a symmetric stretching mode (ν_1), an antisymmetric stretching mode (ν_3), and two bending modes (ν_{2a} and ν_{2b}) which have the same frequency of vibration and form a degenerate pair. These vibrations are shown schematically in Figure 5. The symmetric stretching mode is the only predicted Raman-active vibration because the derivative of the change in total molecular polarizability during this motion is non-zero (see the Appendix for a discussion of Raman theory).

The frequency of the symmetric stretching mode is 1332.87 cm^{-1} (GORDON and MCCUBBIN, 1966). At the same time, in CO_2, this mode has nearly the same energy as the second excited state of an infrared active bending mode ν_2. (see Figure 6) This state, $2\nu_2$, consists of two sublevels ($2\nu_2^0$ and $2\nu_2^2$) that are differentiated based on their symmetry

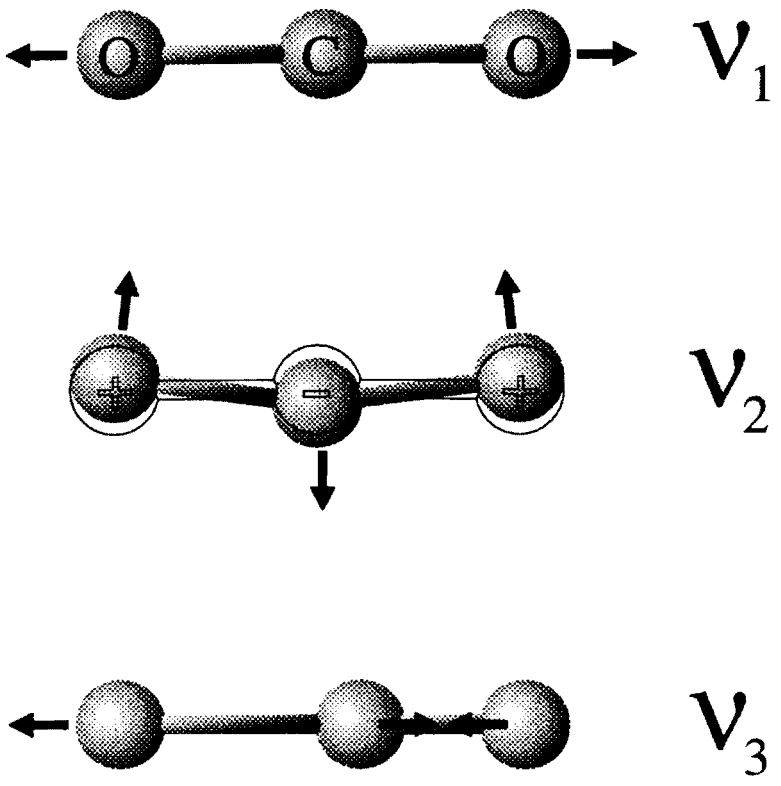

FIGURE 5: Schematic representation of the three fundamental vibrations of CO_2. The only predicted Raman-active mode is the symmetric stretching motion (ν_1). The two mutually perpendicular planes of vibration cause the bending mode (ν_2) to be doubly degenerate.

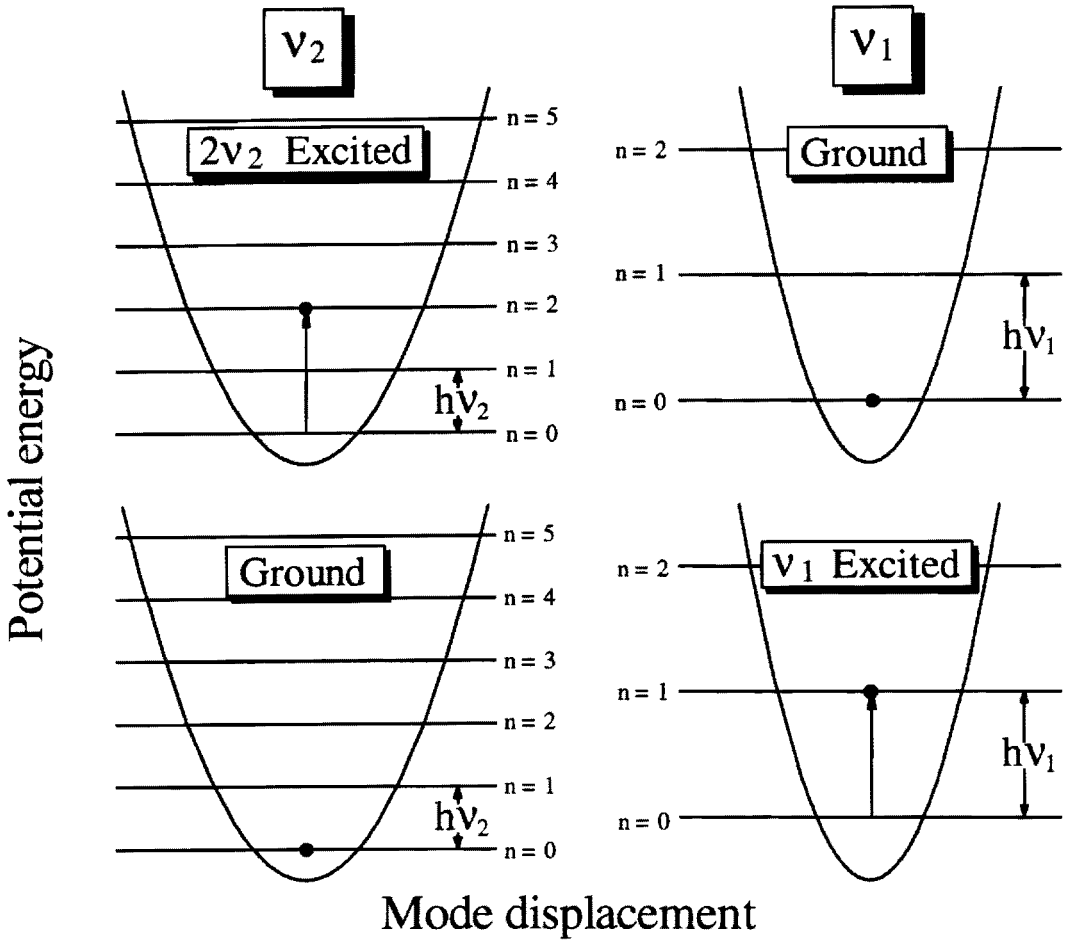

FIGURE 6: Depictions of the potential energy of the excited and ground ν_1 and $2\nu_2$ vibrational states as a function of the mode displacement. For uncoupled excited states, the potential energy is approximately harmonic (parabolic). The width of each parabola is an indication of the vibrational frequency of each mode. Because bond lengths are "stiffer" than bond angles, ν_1 has a higher force constant and a higher frequency than $2\nu_2$. Horizontal lines indicate the vibrational principle quantum number (vibrons). The level spacing is given by $E = (n + 1/2)h\nu$. The vibrational ground state is where $n = 0$. Dots indicate an occupied level. Arrows indicate where the transition originated. Notice that excited states $2\nu_2 \approx \nu_1$. Because the upper two diagrams represent a scenario which cannot be quantum mechanically distinguished from that of the lower two diagrams, the excited states admix.

species (denoted Σ_g^+ and Δ_g respectively) each of which contributes to the symmetry of the bending mode (HERZBERG, 1945). The level $2\nu_2^0$ has a frequency of 1340.74 cm^{-1} (GORDON and MCCUBBIN, 1966). Here, the levels $2\nu_2^0$ and ν_1 are two different vibrational excited states which have nearly the same energy and these are said to be *accidentally* degenerate. Also, these degenerate levels have the same symmetry species (Σ_g^+). Because they accidentally have nearly the same energy and the same symmetry species, they perturb (or repel) each other in the excited state by a process known as Fermi resonance (FERMI, 1931). The perturbation arises from anharmonic vibrational coupling terms (cubic terms) in the potential energy of the molecule, which represent the interaction of the degenerate vibrations (AMAT and PIMBERT, 1965). Because of this anharmonic coupling, the excited $2\nu_2$ level will always excite ν_1 and alternately ν_1 excites $2\nu_2$ such that these excited levels will always admix.

Fermi resonance causes the excited admixed states to split apart. This effect is manifested in the Raman spectrum by the occurrence of two strong CO_2 lines, instead of one, and each is a mixture of the excited ν_1 and $2\nu_2$ levels (Figure 7). These bands are referred to as the ν_1-$2\nu_2$ Fermi diad and have the frequencies 1388.2 cm^{-1} (upper band) and 1285.4 cm^{-1} (lower band) (GORDON and MCCUBBIN, 1966), respectively, at low density (Figure 8). Because these frequencies are a product of the interaction between two vibrational excited states, they cannot be assigned to either ν_1 or $2\nu_2$. However, the relative contribution of each excited state to the upper and lower bands has been studied. Although these relative contributions over a large range of pressures is still under debate, it is generally accepted that the upper band is due dominantly to the excited $2\nu_2$ state and the lower band is due dominantly to the excited ν_1 state in the low density gas (GARRABOS et al., 1989a; 1989b; AMAT and PIMBERT, 1965; GORDON and MCCUBBIN, 1966; HOWARD-LOCK and STOICHEFF, 1971). As will be discussed in a later section, this

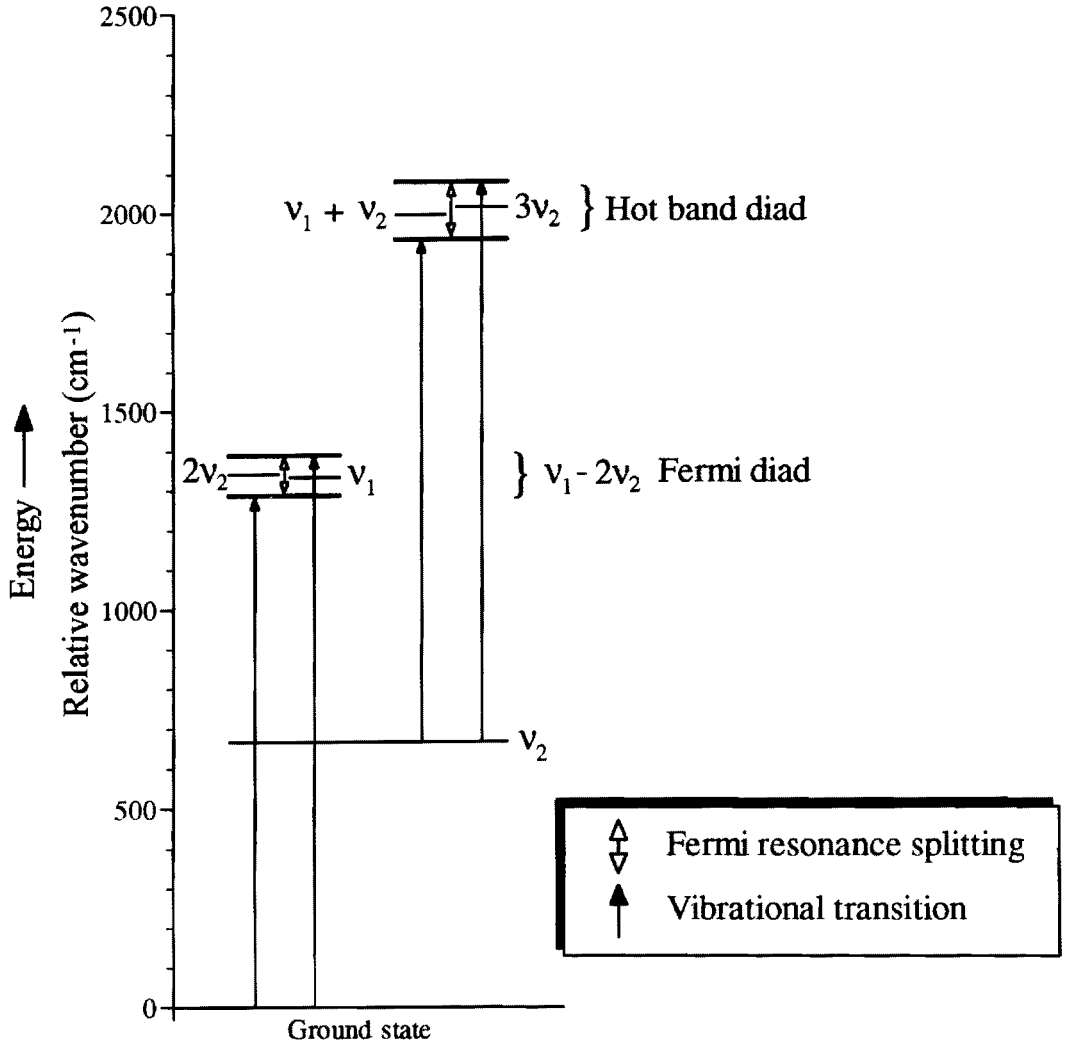

FIGURE 7: Energy level diagram depicting the origin of the CO_2 spectrum. The ν_1-$2\nu_2$ Fermi diad arises from coupling-induced admixture of the ν_1 and $2\nu_2$ vibrational excited states. The resulting bands correspond to the two coupled excitations. In this study they are referred to as simply the upper and lower bands. Hot bands appear as a result of a significant number of molecules populating the first excited vibron of the low-lying ν_2 state at ambient temperature. These are also perturbed by Fermi resonance.

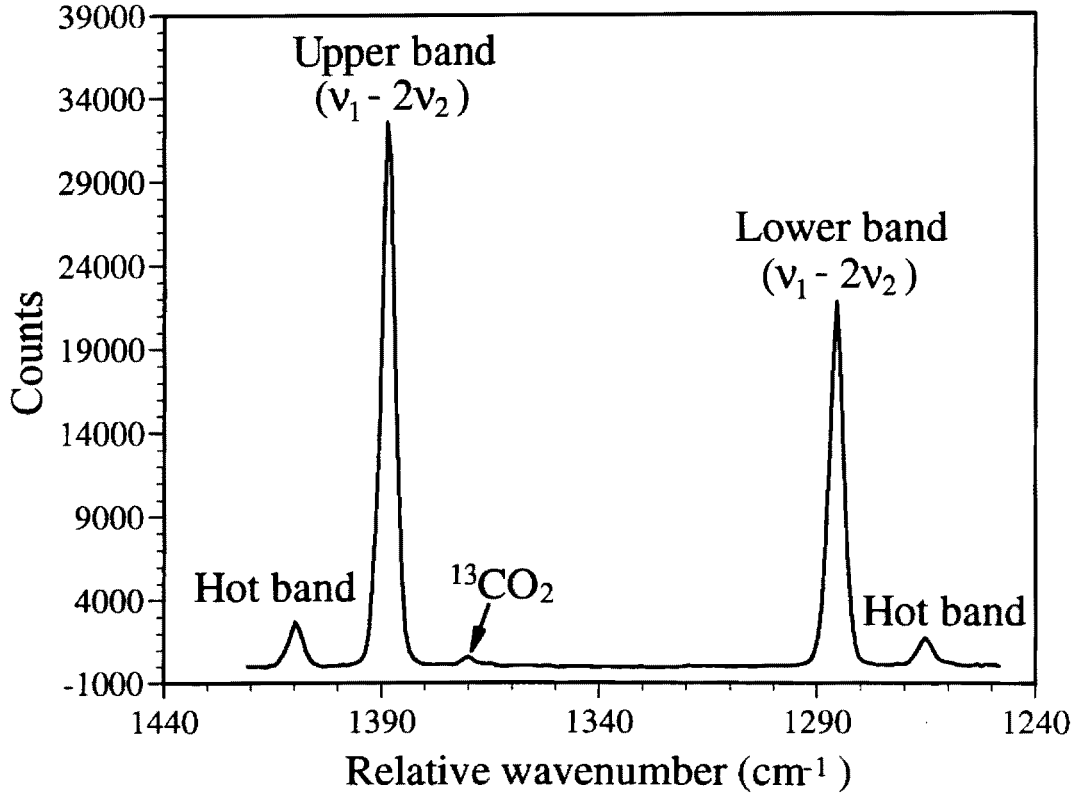

FIGURE 8: Typical Raman spectrum of CO_2 with background subtracted. Peaks marked (ν_1-2ν_2) comprise the ν_1-2ν_2 Fermi diad. The hot bands are also coupled through Fermi resonance.

assignment appears to be reversed at densities above approximately 0.79 g/cm^3 where level inversion occurs at an exact Fermi resonance (GARRABOS et al., 1989b).

Another band type in the CO_2 spectrum is represented by low intensity peaks flanking the Fermi diad, which are referred to as *hot bands*. They arise from transitions that originate in excited vibrational states higher in energy than the ground vibrational state due to the thermal energy of the molecules. The population of these excited states is a function of temperature and the energy difference from the ground state (n = 0). In CO_2, ν_2 is sufficiently low-lying at 667.38 cm^{-1} (GORDON and MCCUBBIN, 1966) (Figure 7) that, at ambient temperature, the population of these states is significant. The hot bands in the CO_2 spectrum result from transitions from ν_2 to levels formed from interactions between $\nu_1 + \nu_2$ and $3\nu_2$ (HERZBERG, 1945) (Figure 9). Similar to the Fermi diad bands, the level $\nu_1 + \nu_2$ (1994.88 cm^{-1}) is nearly degenerate with $3\nu_2$ (2014.48 cm^{-1}) (GORDON and MCCUBBIN, 1966). Thus the hot bands are also perturbed by Fermi resonance. Their resultant frequencies are 1264.8 cm^{-1} and 1409.0 cm^{-1} (DICKINSON et al., 1929) (Figure 8).

The final band type is a very weak peak having a frequency of 1370.0 cm^{-1} (HOWARD-LOCK and STOICHEFF, 1971) (Figure 8). It arises from the isotopic splitting due to the presence of $^{13}CO_2$. In our experiments, natural CO_2 is used. It is known that the $^{13}CO_2$ concentration in natural carbon dioxide is 1.1% on average, therefore, in our experiments, the detection of a very low intensity $^{13}CO_2$ peak is to be expected only at high density.

Raman Detection Limits

The limit of the instrumental capability to detect a substance is related to its net peak intensity (n_{net}), that is, the intensity of the signal of interest above the background

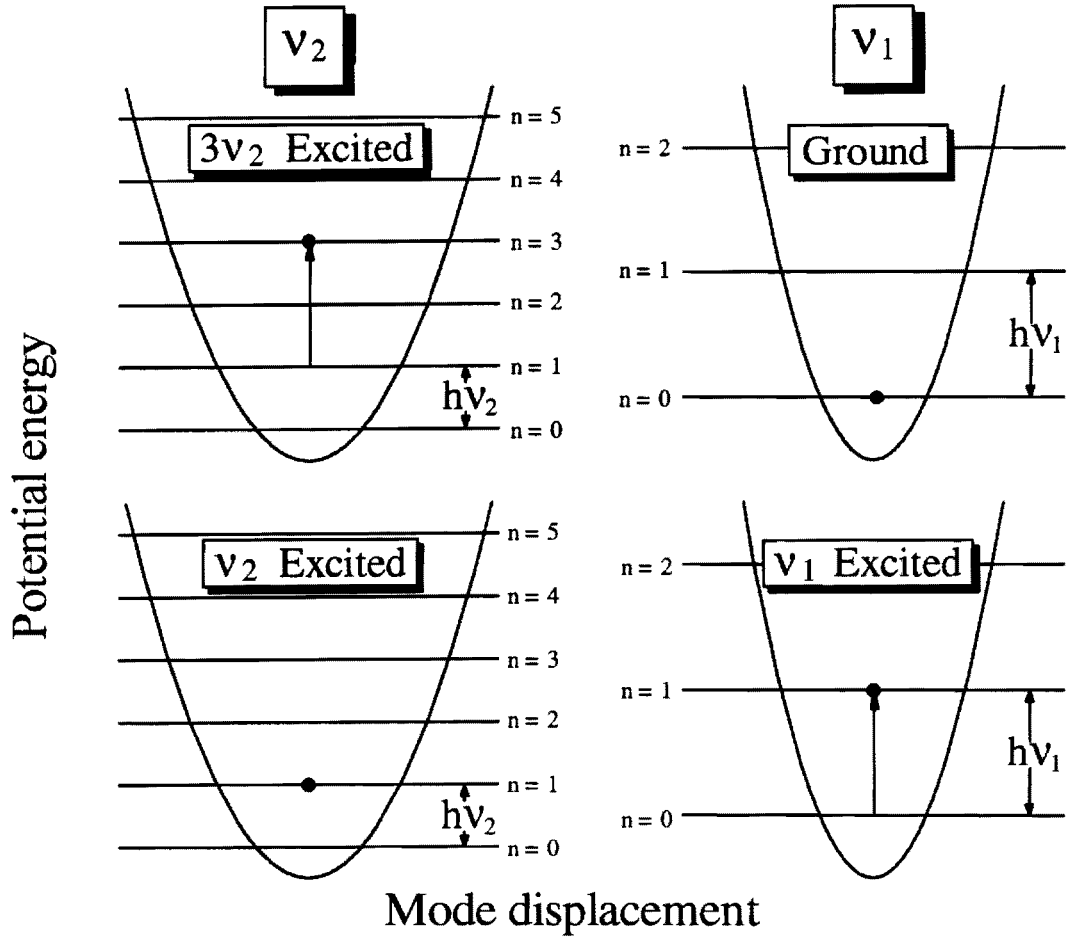

FIGURE 9: Depictions of the excited hot band states. Note that the energy of the $3\nu_2$ excited state is approximately equal to the energy of the $\nu_2 + \nu_1$ excited state. Because the upper two diagrams represent a scenario which cannot be quantum mechanically distinguished from that of the lower two diagrams, the excited states admix.

signal (n_b) of that substance at a particular concentration. Note that here, peak intensity is in terms of the maximum band intensity, not integrated area intensity. The presence of an inherent counting error in the measurement of peak intensity and likewise for the background signal means that we must define our minimum detection limit (MDL) such that a real peak can be distinguished from random fluctuations in the background (noise) (WINEFORDNER and RUTLEDGE, 1985). This error is derived from the Poisson distribution which governs photon counting statistics near detection limits. From this distribution we know that the *standard deviation* (σ) is given by

$$\sigma = \sqrt{\bar{n}} \tag{1}$$

and thus the *variance* is given by

$$\sigma^2 = \bar{n} \tag{2}$$

where n is the number of counts. In our Raman instrument, the background signal is a result of a negligible amount of stray light entering the spectrometer and is predominantly detector dark current. Due to the fact that background counts and counts coming from the sample can be treated as statistically independent distributions, the total variance is equal to the sum of their variances. Thus for net peak counts

$$\sigma^2_{total} = \sigma^2_b + \sigma^2_{net} \tag{3}$$

and

$$\sigma_{net}^2 = \sigma_b^2 + \sigma_{total}^2 = \bar{n}_b + \left(\bar{n}_b + \bar{n}_{net}\right) = 2\bar{n}_b + \bar{n}_{net} \tag{4}$$

where the subscript *total* refers to the sum of the background and the net peak. If we wish to define the signal–to–noise ratio in which the net peak counts are not a result of a statistical fluctuation of the background with 95% confidence (2σ), then

$$n_{net} \geq 2\sigma_{net} \tag{5}$$

and

$$n_{net} \geq 2\sqrt{2\bar{n}_b + \bar{n}_{net}} \tag{6}$$

Assuming that the measured net counts are close to their respective means and are small compared to the background intensity, then we can define the detection limit as

$$n_{net} \geq 2\sqrt{2\bar{n}_b} \cong 3\sqrt{\bar{n}_b} \tag{7}$$

This means that to be 95% confident that a peak is a real detection of a substance, its net count intensity must be 3 times as intense as the square root of the mean background counts. A previous study by WOPENKA and PASTERIS (1987) used a detection limit defined by a signal-to-noise ratio of about two. This corresponds to a confidence interval of about 82%, lower than in the detection limit used here.

In these experiments, the CO_2 density is not directly measured. We monitor the gas pressure at ambient temperature (22°C) and calculate the density using the known real behavior of CO_2. At constant pressure, we expect the peak intensity to show a linear

dependence on both laser power at the sample (proportional to the irradiance) and signal integration time. This means that we can observe how net peak intensity and the background noise change over a range of laser power and integration time settings and project to the minimum detection limits defined by equation 7.

The laser power at the sample was related to the set laser power for the 32x and 80x objective lenses. This was done to determine the relative transmittivities of each objective lens. The results are shown in Figure 10. Also shown is the laser power when the beam is transmitted through the 32x lens and a 1 mm thick glass layer to approximate the effect of the sample capillary tube used in the experiments in this study. The 80x objective lens, used for routine fluid inclusion analyses, transmits ~15% more power than the 32x lens through 1 mm thick glass. Raman intensities are proportional to, among other things, the number of molecules in the excitation volume and the laser power flux (irradiance). Increasing the objective lens power decreases the excitation volume, which decreases the number of scattering molecules and increases the irradiance at the same rate. This means the ratio of Raman intensities resulting from the 80x to the 32x lenses is given by the ratio of their transmitted laser power. Thus, although the CO_2 detection limit is determined using the gas cell and 32x lens, we can expect that this limit will improve by approximately 15% using the 80x objective. The results of these experiments were also used to convert the set laser power to the laser power at the sample.

At various gas pressures up to 60 bars, spectra were collected over four values of laser power and four values of integration time. These values were chosen such that the CO_2 peaks were distinct and well defined. The characteristics of the background in each spectrum were found to be uniform and linear over the range of frequencies observed. The average intensity of the background was recorded and then subtracted from each spectrum. At each CO_2 pressure, a surface was fit to the change in net peak intensity (for

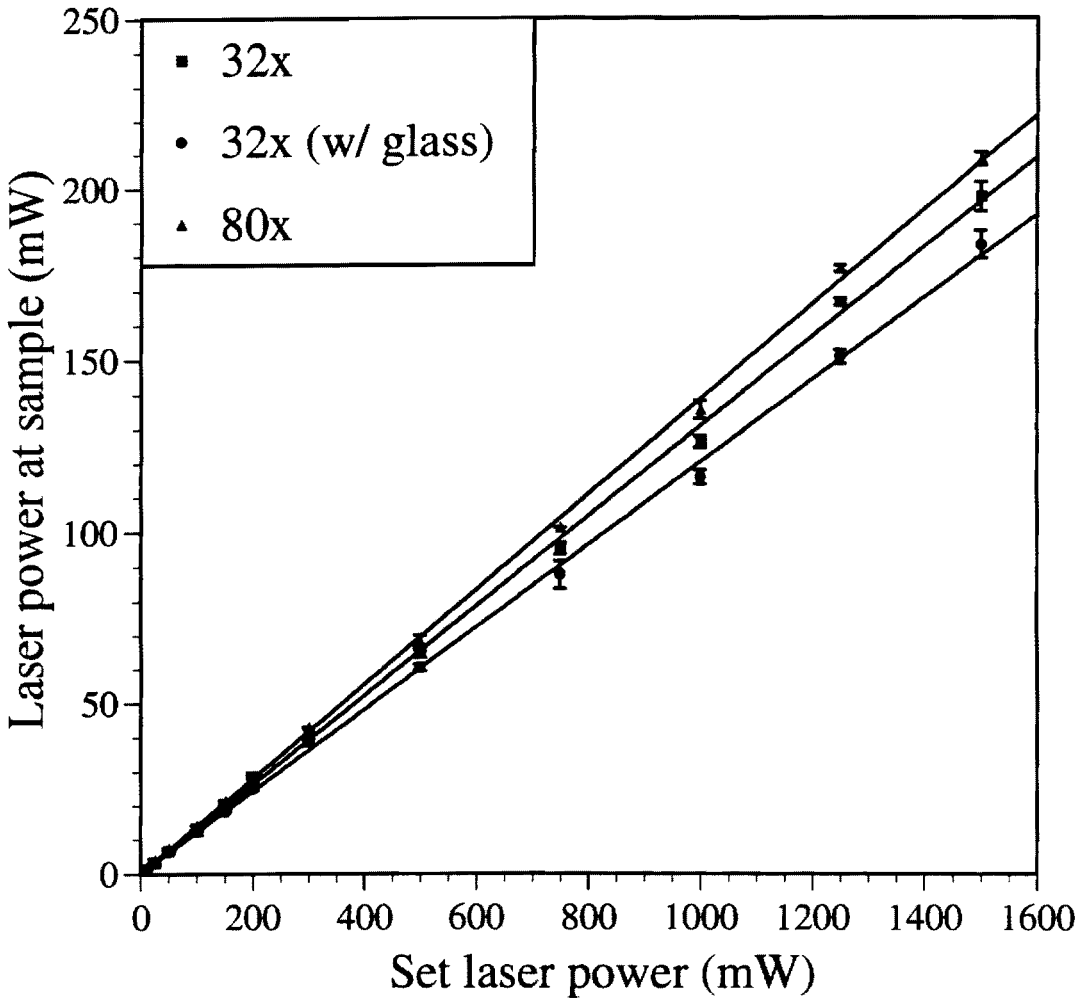

FIGURE 10: The effect of the entrance optics and objective lenses on the laser power reaching the sample. Between 12 - 14% of the set laser power reaches the sample. The relationships are approximately linear within the useful range of laser power. The 80x lens in this study has a 6% higher power transmission than the 32x lens. A 1 mm thick piece of glass decreases the throughput of the 32x lens by 8%. Error bars are 3 std. dev. of the mean (n = 3).

each Fermi diad band) as a function of integration time and laser power. The basic form of the surface equation is

$$Z_n = Ax + By + Cxy + D \tag{8}$$

where Z_n is the net peak intensity, x is integration time, y is laser power, and A, B, C, and D are the fitting parameters. This equation expresses intensity as a linear function of integration time when laser power is constant, and vice versa. However, because we have the restriction that there can be no intensity (except for the floating parameter D) when either integration time or laser power is zero, the A and B parameters are assumed to be zero and the equation reduces to

$$Z_n = C_n xy + D_n \tag{9}$$

Each surface was fit utilizing a least squares method. A datum weighting scheme was derived using the estimated intensity errors of each datum as weights.

The least squares estimates of the D_n parameter, which is the theoretical net peak intensity when the integration time and laser power are zero, were taken as the average of those in the $2\nu_2$ set and in the ν_1 set. This is because for a particular CO_2 band, we would expect that this intercept value would be the same, independent of CO_2 pressure.

The detection limit $(3(n_b)^{1/2})$ can also be expressed as a surface in intensity, integration time, and laser power space. The shape and position of this surface is dependent on the behavior of the average background intensity. It turns out that the background intensity has an additional degree of freedom as compared to the behavior of the net peak intensity. The background intensity increases with integration time regardless

of the laser power. This is due to the inherent thermionic dark current level in the detector which depends on the signal integration time. Thus the background intensity (Z_b) can be expressed as

$$Z_b = Ax + Cxy + D \tag{10}$$

where A equals the change in background intensity with integration time, independent of laser power. From this we can derive the general expression for the detection limit surface (Z_d)

$$Z_d = 3(A_d x + C_d xy + D_d)^{1/2} \tag{11}$$

The derivation of the parameters in Z_d, however, is not trivial because Z_d does not have a linear dependence on integration time or laser power. These parameters were determined analytically. The intersection of the surface Z_d and each net peak intensity surface, Z_n, gives an equation of a line which is an MDL isobar. Plots of these isobars for the $2\nu_2$ and the ν_1 bands are shown in Figure 11 at 22°C.

In addition to determining detection limit isobars, the linear relationship between intensity and CO_2 density was used to extrapolate to the detection limit density for particular instrumental settings. These results were combined with the isobar data of Figure 11 (converted to isochores) to determine the MDL as a function of density. The resulting MDL surfaces for both the $2\nu_2$ and ν_1 bands are shown in Figure 12. The surfaces are formed by plotting integration time isochrons as a function of minimum CO_2 density and laser power at the sample. The nature of the surface is that rapid changes in the detection limit occur at laser power values less than about 50 mW. At higher values,

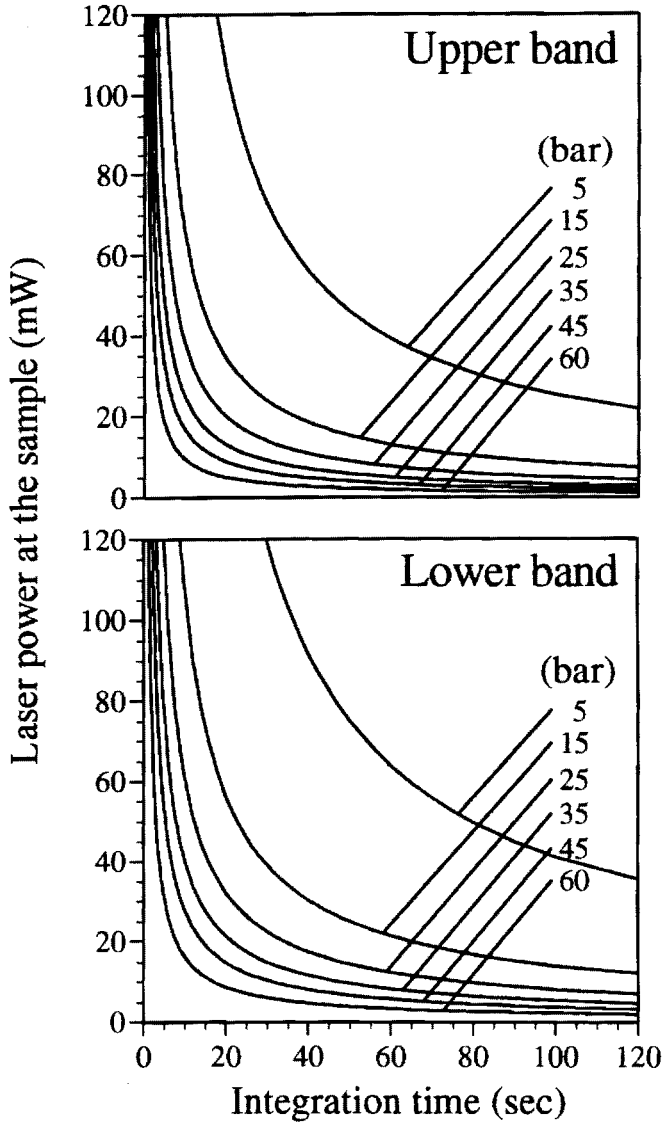

FIGURE 11: Detection limit isobars for the upper and lower bands of the ν_1-$2\nu_2$ Fermi diad at 22°C on the high pressure (> 5 bar) side of the detection limit surface. Both plots show that increasing the integration time to longer than 120 seconds and the laser power at the sample to more than 120 mW does not significantly improve the detection limit.

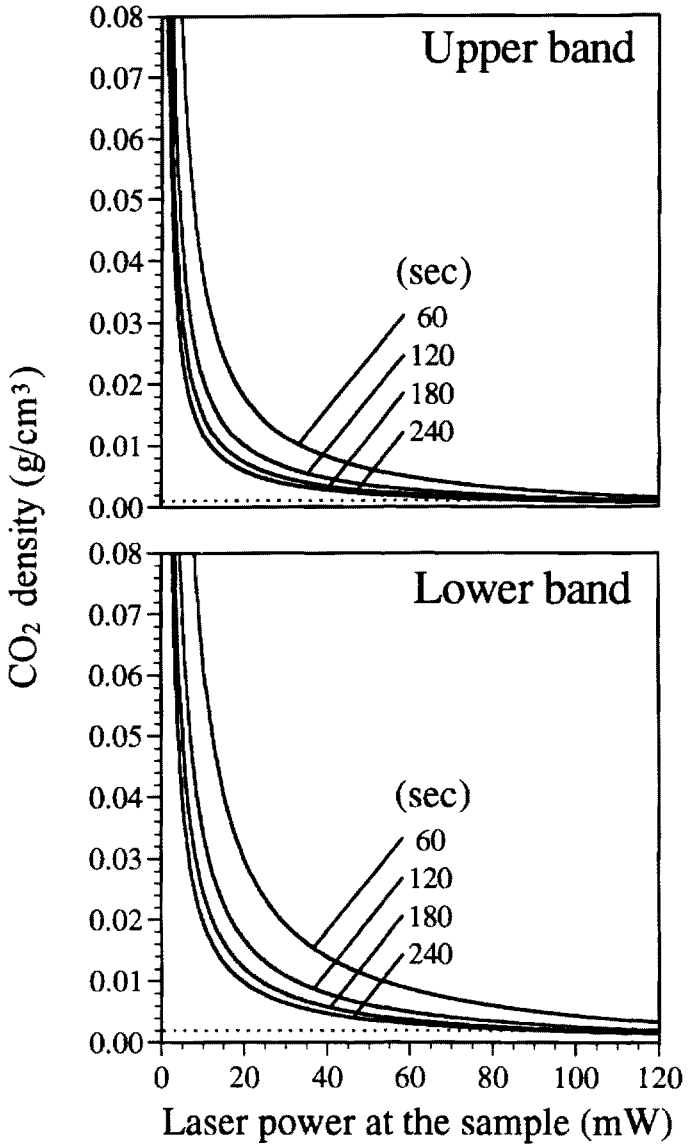

FIGURE 12: Detection limit surface for the upper and lower bands of the ν_1-$2\nu_2$ Fermi diad. Isochrons (solid curves) project asymptotically to a constant density at infinite laser power, however the practical laser power limit with fluid inclusions is approximately 100 mW at the sample. At 240 sec. and 100 mW at the sample, the estimated detection limit is 0.5 bar for the upper band and 1.0 bar for the lower band.

the detection limit changes very slowly with integration time and laser power such that, for all practical purposes, it asymptotically approaches a constant value. Using the 120 sec isochron at 100 mW, the detection limit can be estimated to be approximately 0.5 bar for the upper band and 1.0 bar for the lower band.

Band Shift

The characteristics of Raman bands, such as frequency, shape, and intensity, are dependent on the rate of change of the molecular polarizability during a vibrational motion. The polarizability is an intrinsic property of each molecule which is a measure of the facility with which it can induce a dipole moment in an electromagnetic field. The frequency and amplitude of oscillation of the induced dipole can be influenced by the molecular environment surrounding a molecule. Thus, changes in band characteristics are interpreted in terms of molecular interactions which affect a vibration.

In the spectrum of CO_2, the bands of the Fermi diad shift to lower frequencies (or wavenumber) with increasing density. The frequency shift of the lower band has a higher density dependence than does the upper band. At the same time, the intensity ratio of the upper band to the lower band increases with increasing density (GARRABOS et al., 1980) (see Figure 13). Normally, shifts in band frequency can be directly related to changes in the molecular environment, such as changing the number of intermolecular collisions which is a function of, among other things, density. However, in the case of CO_2, the behavior of band shifts and intensity changes are complicated by Fermi resonance. The admixture of the $2\nu_2$ and ν_1 excited states means that the individual $2\nu_2$ and ν_1 excited states do not exist. Although this is true for the density range studied here, we can describe what would be happening to the individual $2\nu_2$ and ν_1 excited states by using the known nature of the coupling phenomenon.

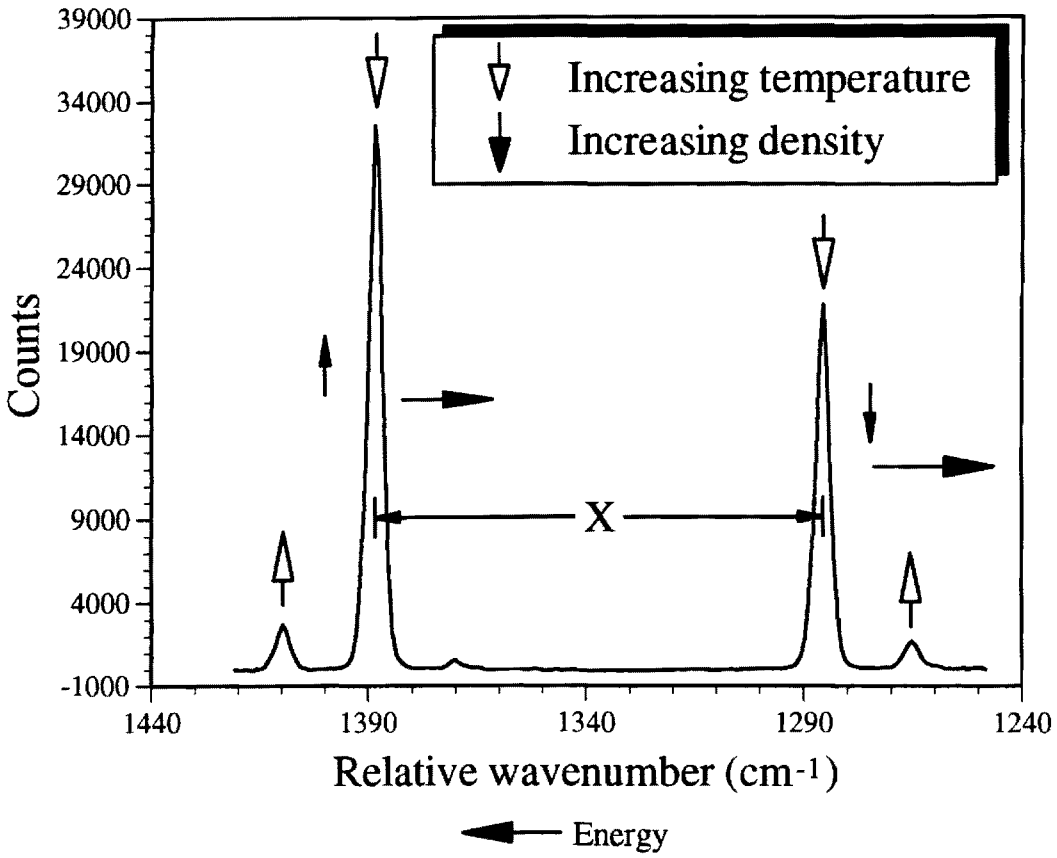

FIGURE 13: The relative effects of temperature and density on the spectrum of CO_2. The arrow size is proportional to the magnitude of an effect on a band. Fermi diad bands shift to lower wavenumber with increasing density. The lower band shifts more rapidly than the upper band. The splitting between these two bands (*X*) is a linear function of density in the range observed in this study (see Figure 14). The intensity ratio of the upper to lower band increases slightly with density, but their summed intensity is constant. The intensity ratio of the hot bands to the ν_1-$2\nu_2$ Fermi diad increases with increasing temperature (see Figure 16).

The relationship between the magnitude of the resonance splitting ($X = \nu_u - \nu_l$) of the observed upper and lower bands of the Fermi diad and the separation of the unperturbed (uncoupled) levels ($\delta = \nu_1 - 2\nu_2$) is given by

$$X = \nu_u - \nu_l = \left(\delta^2 + 4W^2_{\nu_1,2\nu_2}\right)^{1/2} \tag{12}$$

where W is the Fermi coupling constant which arises from anharmonic terms in the potential energy (HERZBERG, 1945). Equation 12 shows that an increase in resonance splitting is due to an increase in the magnitude of the separation of the unperturbed excited levels and/or the magnitude of W. Experimental observations of the density dependence of X and W allow estimations of density related changes in δ. Thus, we can interpret observed relative band shifts in terms of corresponding relative shifts in the theoretical unperturbed excited levels $2\nu_2$ and ν_1 in CO_2.

Figure 14 shows the density dependence of resonance splitting (X) determined from this study and compares the results to those of GARRABOS et al. (1980, 1989a). Our data were taken separately in gas and liquid phase CO_2 below the critical temperature (31.1°C) at approximately 22°C whereas the data of GARRABOS et al. were taken at 40°C. Thus we were not able to collect data in the density range of phases along the coexistence curve. The temperature effect on X can be assumed to be negligible (GARRABOS et al., 1989b). GARRABOS et al. (1989a; 1989b) achieve a better fit to their data using a second-order polynomial function; however, the scatter in their data does not allow one to adequately differentiate second-order versus linear behavior. For the purposes of this study, and due to the good agreement between the data sets shown in Figure 14, the relationship between X and density is assumed to be linear in this density range.

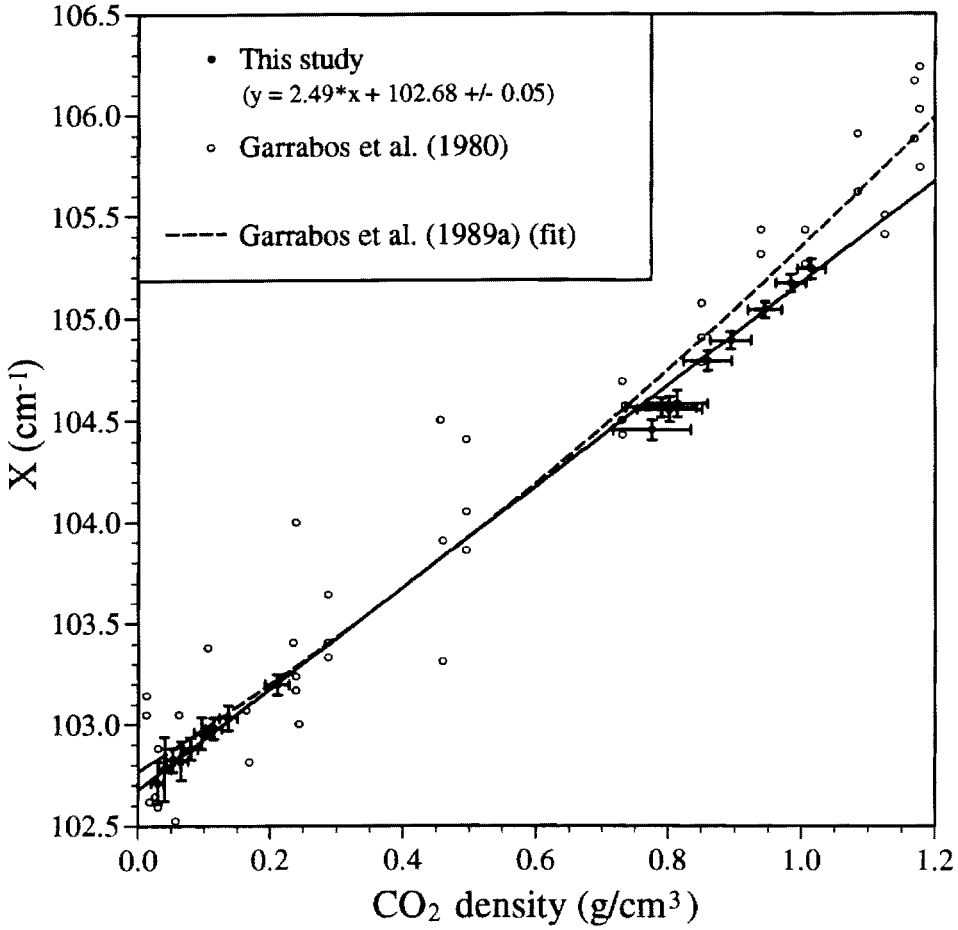

FIGURE 14: The Fermi resonance splitting (X) between the upper and lower bands. The lower density cluster of data was collected in the gas phase (< 0.5 g/cm^3) and the upper cluster in the liquid phase (> 0.5 g/cm^3) (at 22°C). Errors bars were derived from the quadratic sum of the fractional uncertainty contributions. The data were least-squares fit using density errors as weights. The data are compared to the work of GARRABOS et al. (1980, 1989a).

Our data were least-squares fit with an error weighting scheme based on the estimated uncertainty in the calculated density. The fractional density uncertainty ($\delta\rho$) was calculated using a quadratic error propagation formula, given below, including the fractional uncertainties in the temperature (δT), pressure (δP), and the estimated uncertainties (δF) in the CO_2 equations of state (DUSCHEK et al., 1990; BOTTINGA and RICHET, 1980)

$$\delta\rho/\rho = \sqrt{(\delta T/T)^2 + (\delta P/P)^2 + (\delta F/F)^2} \tag{13}$$

The resulting uncertainties represent one standard deviation. The uncertainty in X was determined by summing the errors corresponding to the determination of the individual upper and lower band positions. For bands which are symmetrical and resolved, as are the bands in this study, the determination of band frequencies is not influenced by the spectral resolution (SEITZ et al., 1993). Also, because spectra of the Fermi diad bands can be collected simultaneously, frequency errors introduced by temperature fluctuations in the spectrometer and instrumental drift negate each other. The primary uncertainty arises from the confidence limits of the peak center derived from the individual peak fitting algorithm. These were calculated by taking the square root of the diagonal elements of the covariance matrix for the peak center parameter. The results are the standard errors of the fit which were on the order of 0.01 cm^{-1} for each band. The overall precision of the determination of X is approximately ± 0.05 cm^{-1} which equates to ± 0.02 g/cm^3.

In early studies of the low density gas phase, W was assigned a value of -51.232 cm^{-1} and δ was assigned a value of -7.87 cm^{-1} in accordance with $2\nu_2 > \nu_1$ (GORDON and MCCUBBIN, 1966; HOWARD-LOCK and STOICHEFF, 1971) Subsequent studies which attempted to determine the density dependence of δ assumed that W was essentially

density independent (WRIGHT and WANG, 1973; WANG and WRIGHT, 1973; BERTRAN, 1983). However, it has been demonstrated by GARRABOS et al. (1989a; 1989b) that both δ and W are slightly density dependent. It was argued that this must be so in order explain band assignment contradictions between the low and high density phases. Their work showed that δ increases with increasing density to approximately 0.79 g/cm^3 (GARRABOS et al., 1989b) where $\delta = 0$. At this point, an exact Fermi resonance occurs ($2\nu_2 = \nu_1$) and *X* is determined by 2|W|. At higher density, the band assignment is reversed such that the upper band is dominantly ν_1 and the lower band is dominantly $2\nu_2$. This density dependence of δ can be illustrated using the known low density value of W at $\rho = 0$ and the point of exact Fermi resonance ($\delta = 0$) at $\rho = 0.79$ g/cm^3. Assuming for the moment that $\delta << 2|W|$ and that the density dependence of W can be approximated by a straight line, we can plot 2|W| along with the trend of *X* measured in this study using the points discussed above (Figure 15a). The disagreement between the two lines represents the influence of δ. Due to the uncertainties in *X* and W and the similarities in the slopes of these lines, an accurate determination of δ is not possible here. However, it can be stated with reasonable certainty, that for the relation between *X*, δ, and W to hold, δ must increase (from -7.87 cm^{-1}) with density. This means that the energy difference between the unperturbed levels $2\nu_2$ and ν_1 approaches zero as density is increased from low density to approximately 0.79 g/cm^3. At higher densities, δ continues to increase due to an increasing separation of the unperturbed levels. The calculated positions of the unperturbed $2\nu_2$ and ν_1 levels from GARRABOS et al. (1989b) is shown in Figure 15b. Here it can be seen that, theoretically for the uncoupled excited $2\nu_2$ and ν_1 states, $2\nu_2$ demonstrates a much greater density dependence than ν_1. The state $2\nu_2$ decreases monotonically with increasing density. The state ν_1 displays a slight frequency decrease and then an increase with increasing density. Although the theoretical details have never

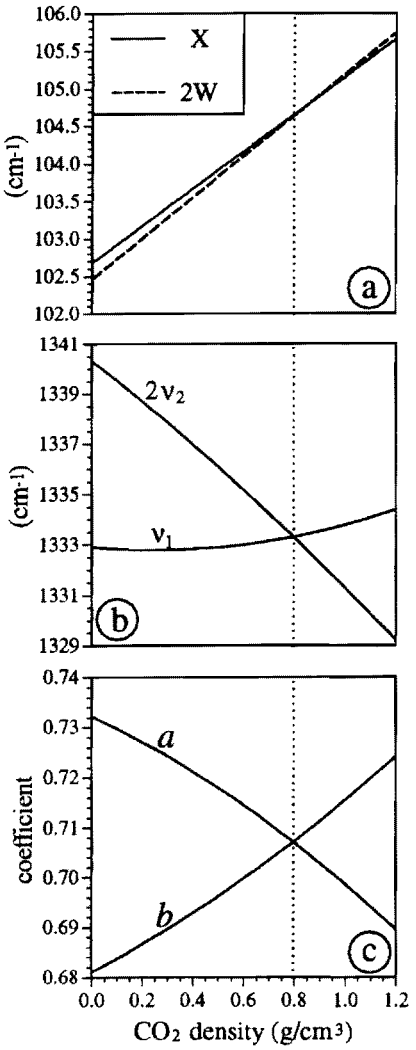

FIGURE 15: (a) The fit to resonance splitting data of the ν_1-$2\nu_2$ diad (*X*) data measured in this study compared with twice the Fermi coupling constant (W). The trend of W was inferred from the known value at low density, the condition 2W = X at ~0.8 g/cm^3, and a linear approximation. The difference between the two slopes is due to the effect of δ (see equation 12 in the text) which is the separation of the theoretical unperturbed levels. (b) Density dependent frequency shifts of the theoretical unperturbed ν_1 and $2\nu_2$ levels from GARRABOS et al. (1989b). $2\nu_2$ changes much more rapidly than ν_1. The initial frequency decrease in ν_1 may be a result of the mean contribution of intermolecular attractive forces while the higher density frequency increase is related to intermolecular repulsion (MAY et al., 1961). (c) The mixing coefficients *a* and *b* (see equations 14-17 in the text) as a function of density. These demonstrate the proper low density band assignment where the lower band is dominantly due to ν_1 and the upper band dominantly $2\nu_2$. Exact Fermi resonance occurs at about 0.8 g/cm^3 (GARRABOS et al., 1989b). The higher density assignment is reversed from low density.

been studied (WRIGHT and WANG, 1974), it can generally be stated that the initial ν_1 frequency decrease is a manifestation of the mean contribution of intermolecular attractive forces at low density. At higher density, the frequency increase reflects the dominance of the intermolecular repulsive force contribution (MAY et al., 1961). At low densities, the separation between $2\nu_2$ and ν_1 decreases with increasing density, which couples the Fermi diad. The increasing separation at high densities causes a decrease in the degree of resonance coupling and tends to decouple the Fermi diad (WANG and WRIGHT, 1973).

The degree of resonance coupling of the perturbed upper and lower states can be determined by examination of their respective eigenfunctions (HERZBERG, 1945) which are given by

$$\psi_u = a\psi_{\nu_1} - b\psi_{2\nu_2} \tag{14}$$

$$\psi_l = b\psi_{\nu_1} + a\psi_{2\nu_2} \tag{15}$$

where

$$a = \left(\frac{X+\delta}{2X}\right)^{1/2} \tag{16}$$

$$b = \left(\frac{X-\delta}{2X}\right)^{1/2} \tag{17}$$

The coefficients a and b were calculated using the density dependence of X measured in this study and the trend for δ from GARRABOS et al. (1989b) and are shown in Figure 15c. The low density band assignment is correctly represented with the upper band dominated

by the state $2\nu_2$ and the lower band due mostly to the state ν_1. As density increases, the coefficient *a* continually increases while *b* decreases. This translates into a gradual change in the mixture of the perturbed bands. With increasing density, the upper band assumes less $2\nu_2$ character and more ν_1 character while the lower band assumes more $2\nu_2$ and less ν_1 character. This means that, as density approaches 0.79 g/cm^3, the Fermi diad gradually becomes more coupled. At 0.79 g/cm^3, each of the perturbed upper and lower bands are half due to $2\nu_2$ and half due to ν_1. At higher densities, the band assignment is reversed such that the upper band is dominantly ν_1 and the lower band is dominantly $2\nu_2$, achieving the correct high density band assignment. At the same time, δ increases in magnitude and gradually decouples the Fermi diad. This behavior is consistent with the known intensity ratio trend of the upper to lower bands in the CO_2 spectrum, which increases with density. This is because, as density increases, a larger fraction of the intense ν_1 excited state is shifted from the lower band to the upper band while the weaker $2\nu_2$ excited state is shifted from the upper band to the lower band. This also implies that the sum of the upper and lower band intensities remains the same, regardless of density.

Hot bands

Raman band intensities are generally proportional to, among other things, the number of molecules in the scattering volume or the density (LONG, 1977). The excitation of a molecular vibration can be regarded as the promotion of a molecule from its current vibrational state to a higher vibrational state (Stokes). In most cases at ambient temperature, the dominant unexcited vibrational state is the ground state of the molecule which corresponds to zero vibrational energy. Therefore, most Raman bands are those that arise from transitions from the ground state to an excited state. However, from

statistical thermodynamics, it is known that within a population of molecules there are certain portions of the molecules in excited states due to the temperature of the sample. Therefore, it is possible for Raman transitions to arise from these thermally excited states to other higher excited states. If the population of the thermally excited states is significant, it is possible for these bands to be detected in the Raman spectrum. These bands are referred to as difference bands or, more commonly, *hot bands*.

The population distribution of the vibrational states of an assemblage of molecules is governed by the Boltzmann distribution law. This states that, at thermal equilibrium, the mean number of molecules N_i in a given state i of energy ε_i of degeneracy ω_i is proportional to

$$\omega_i \, e^{-\varepsilon_i / kT} \tag{18}$$

where k is the Boltzmann constant (1.38×10^{-23} J/K) and T is temperature in Kelvin. Simply stated, N_i is proportional to the probability of the energy level i to which it refers. The ratio of the population numbers of two levels ε_i and ε_j is obtained from

$$\frac{N_i}{N_j} = \frac{\omega_i \, e^{-\varepsilon_i / kT}}{\omega_j \, e^{-\varepsilon_j / kT}} \tag{19}$$

which is an equality because the probability of each of the two levels is taken to be the same. If we assign the level j as the vibrational ground state ($\varepsilon_j = 0$, $\omega_j = 1$), then we can predict the distribution of molecules in an energy state higher than the ground state (*GS*) as

$$\frac{N_i}{N_{GS}} = \omega_i e^{-\varepsilon_i/kT} \tag{20}$$

For the purposes of Raman spectroscopy, we commonly refer to energy states in units of relative wavenumber and it can be shown that

$$\frac{N_i}{N_{GS}} = \omega_i e^{-hc\nu_i/kT} \tag{21}$$

where h is Planck's constant (6.63 x 10^{-34} J·sec), c is the speed of light (3.00 x 10^{10} cm/sec), and ν is the frequency of the Raman shift (cm^{-1}). As can be seen in the above relationship, the closer the energy of an excited state is to the ground state, the higher is the population ratio.

In the vibrational spectrum of CO_2, the lowest lying excited state is the level ν_2 at 667.38 cm^{-1} (GORDON and MCCUBBIN, 1966) which is also doubly degenerate ($\omega_{\nu_2} = 2$). This equates to a population ratio of about 0.08 at 25°C. Although this ratio is significant, a Raman band will not be observed in the spectrum unless the fraction of the excited molecules occupying ν_2 can be further excited across a Raman allowed transition. In CO_2, these molecules are excited to a level in which both ν_2 and ν_1 are excited ($\nu_1 + \nu_2$) (HERZBERG, 1945) (Figure 9). In the simple sense, because the transition involves only the excitation of ν_1, the transition $\nu_2 \rightarrow \nu_1 + \nu_2$ is allowed and should have the same frequency as ν_1. However, this does not occur because for CO_2, where $\nu_1 \approx 2\nu_2$, the level $\nu_1 + \nu_2$ (1994.88 cm^{-1}, Gordon and McCubbin (1966)) is nearly degenerate with the level $3\nu_2$ (2014.48 cm^{-1}). These excited levels also have the same symmetry species (Π_u) which results in another Fermi diad in the spectrum of CO_2. At low densities, the magnitudes of

δ and W for this diad are larger than for the ν_1-$2\nu_2$ diad, resulting in a greater splitting of the perturbed levels for the hot band diad (Figure 7). Thus, the frequency of the hot bands does not coincide with the ν_1-$2\nu_2$ diad and are observable in experiments.

Due to the fact that transition from ν_2 to $\nu_1 + \nu_2$ requires only the excitation of ν_1, the transition probability is the same as that for the excitation of ν_1 from the ground state. This means that the intensity ratio of these two transitions is approximately equal to the population ratio of molecules in the ν_2 excited state to those in the ground state. For both diads, the observed intensity of each of these transitions is diminished by the transfer of energy to their corresponding resonance levels. However, the intensity sum of the two bands in each diad circumvents the effects of Fermi resonance on the intensity ratio.

In order to apply the Boltzmann factor relationship to Raman band intensities, the known intensity behavior of radiative emissions, which varies with the fourth power of the frequency of the emitted radiation, must be taken into account. In the case of the CO_2 spectrum, the frequencies of each of the bands are corrected for in the following expression of the intensity ratio of the summed hot bands to the summed ν_1-$2\nu_2$ diad

$$\frac{I_{HB}}{I_{FD}} = \frac{\left[(\nu_0 - \nu_{uHB})^4 + (\nu_0 - \nu_{lHB})^4\right]}{\left[(\nu_0 - \nu_u)^4 + (\nu_0 - \nu_l)^4\right]} \omega_{\nu_2} e^{-hc\nu_2/kT} \qquad (22)$$

where I is intensity instead of simply the number of molecules in a given state, ν_0 is the frequency of the incident radiation, ν_{uHB} and ν_{lHB} are the observed frequencies of the upper and lower hot bands (*HB*), and the subscript *FD* refers to the ν_1-$2\nu_2$ Fermi diad. In this case, where the band positions of the upper bands of both diads have similar

frequencies and likewise for the lower bands, the frequency factor has a negligible influence on the intensity ratio.

The relative band intensities of the upper and lower bands of each diad change as a function of density. Because these diads are distinct, the rate of this change is most likely not the same for both diads. This precludes determining density independent ratios of the upper bands and the lower bands separately. In this study, the bands of each diad were summed in order to be used independently of the density of the sample. The results are shown in Figure 16. The data were fit using the Boltzmann factor model described above, neglecting the frequency factor, and letting the ν_2 frequency vary as the fit parameter. The resulting value for ν_2 was 669.5 cm^{-1} which compares well with the reported value of 667.38 cm^{-1} (GORDON and MCCUBBIN, 1966). In order to facilitate the comparison, the calculated temperature dependence is plotted using the ν_2 value of GORDON and MCCUBBIN (1966). The relationship is nearly linear in the temperature range used in this study and it has been shown to be nearly linear at high temperatures (WIENECKE et al., 1986) although other increasingly more populated excited states result in hot bands which overlap with those discussed here.

The data in Figure 16 represent the average values of three trials, the standard error of which was on the order of 0.0001. However, three trials is not an adequate sample for a determination of the intensity ratio uncertainty. Therefore, propagated uncertainties were used to estimate the standard error. The fractional uncertainty in the intensity ratio (δI) was calculated for each datum by using the uncertainties in peak counts (δC_{HB} and δC_{FD}) and the average peak intensity fitting uncertainty (δQ) as follows

$$\delta I/I = \sqrt{(\delta C_{HB}/C_{HB})^2 + (\delta C_{FD}/C_{FD})^2 + (\delta Q/Q)^2} \qquad (23)$$

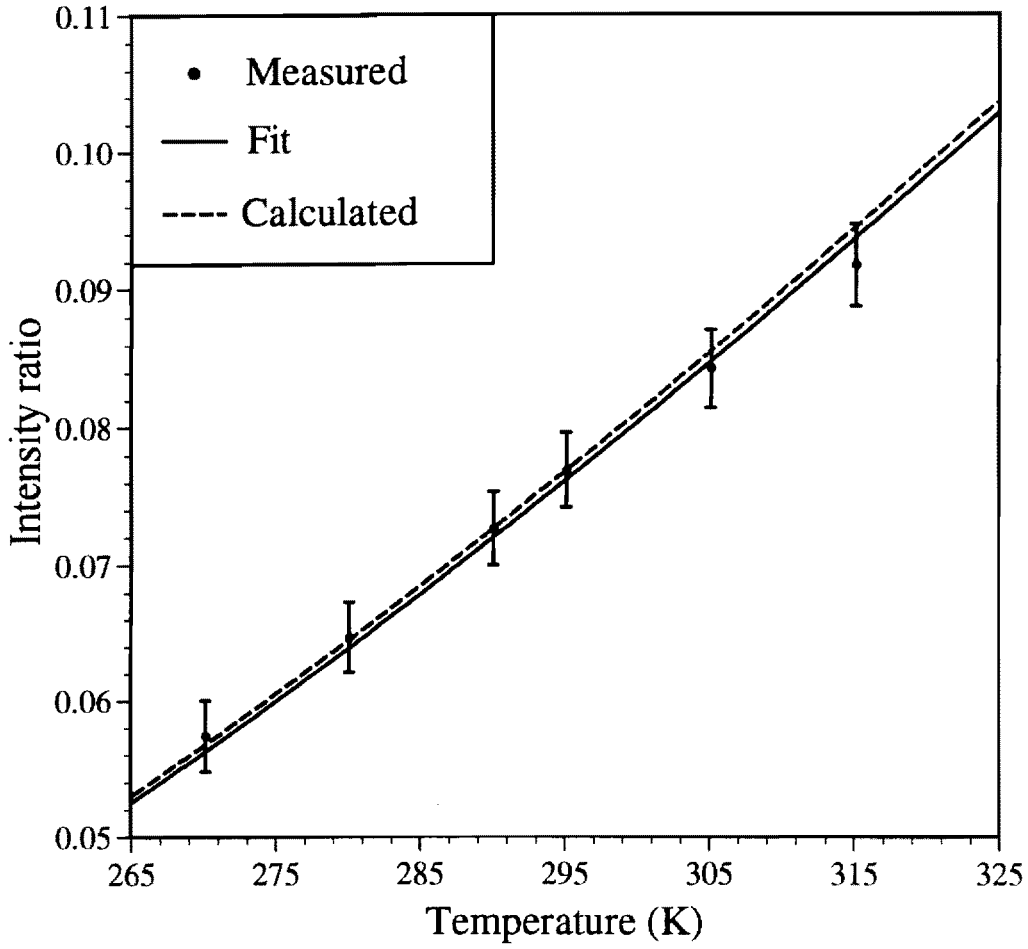

FIGURE 16: Intensity ratio of the summed intensities of the hot band diad to the summed intensities of the ν_1-$2\nu_2$ Fermi diad bands. Error bars were derived from the quadratic sum of the fractional uncertainty contributions. Both the calculated and fit trends are based on the Boltzmann factor model. The calculated trend (dashed line) uses the literature value of 667.38 cm^{-1} (GORDON and MCCUBBIN, 1966) for ν_2. The fit to the data in this study (solid line) results in ν_2 = 669.5 cm^{-1}. This agreement indicates that there is no detectable discrepancy between the temperature of the sample in the excitation volume and the surrounding temperature.

where the uncertainty in the peak counts is taken to be the square root of the peak plus background counts (see equation 3). The resulting uncertainties represent one standard deviation.

Within the temperature range measured in this study, the observed and calculated trends agree within the estimated experimental error. The slight difference may represent an effect of Fermi resonance which is not accounted for in the expression for the intensity ratio (HERZBERG, 1945). The otherwise close agreement between the observed and calculated trends indicates that the temperature of the sample in the stage is not different from the temperature of the gas in the excitation volume. That is to say that laser induced heating of the molecules in the excitation volume is not significant. Additionally, these results indicate that this intensity ratio can be used to estimate the sample temperature.

Summary

The results presented in this study indicate that the detection limits for CO_2 in fluid inclusions using microthermometry require an internal pressure of at least 10.4 bars to observe clathrate dissociation. In an H_2O-CO_2 inclusion having P_{CO_2} = 10 bars at 25°C, and a liquid to vapor volume ratio of 1, a bulk CO_2 concentration of 1.3 mole% can be overlooked during a routine microthermometric analysis. If this fluid were trapped in a hydrothermal system at 250°C, this neglect would result in an estimation of the depth of the two phase field which is about 79% less than the actual value (BODNAR et al., 1985).

Using Raman spectroscopy, CO_2 can be detected to about 1 bar at ambient temperature. In the example above, if we adjust the internal pressure to 1 bar, the resulting undetected bulk CO_2 concentration is only 0.13 mole% and the depth estimation of the two phase field, neglecting CO_2, is only 17% less than the actual value.

Determination of the CO_2 density using microthermometry requires that the CO_2 homogenization temperature can be observed. In low bulk density and/or low bulk CO_2 concentration inclusions, CO_2 homogenizes to the vapor phase, and previous studies have documented the poor precision with which this can be measured (STERNER and BODNAR, 1991). This study shows that to condense liquid CO_2 at low temperatures where it contributes to an observable solid CO_2 melting event, the sample must contain at least approximately 45 bars CO_2 at 25°C.

CO_2 densities can be determined using the ν_1-$2\nu_2$ band separation in the Raman spectrum. This technique can be utilized on individual homogenous gas or liquid CO_2 phases up to about 1.2 g/cm^3. In cases where both liquid and gaseous CO_2 are present at ambient temperature, spectra can be recorded at temperatures higher than the CO_2 critical point in order to ensure that a homogeneous phase is being measured.

In those samples where densities are not near the detection limits of the instrument, hot bands will appear in the spectrum. The intensity ratio of the summed hot band diad to the ν_1-$2\nu_2$ diad will give an estimation of the sample temperature. This temperature should correspond well with the estimated environmental temperature surrounding the sample. This temperature dependence has been calculated using the Boltzmann factor relationship in the temperature range of this study.

Using Raman spectroscopy, the low detection limits of CO_2 allow one to characterize these phases over a larger range than using microthermometry. Density and temperature measurements can be obtained simultaneously in individual spectra. These parameters can be used in conjunction with an appropriate equation of state for CO_2 in order to determine P_{CO_2}.

APPENDIX

Raman Spectroscopy

When molecules of a substance are illuminated with monochromatic light, a small proportion, about 10^{-3}, of the incident light is elastically scattered (Rayleigh scattering). A smaller proportion, usually 10^{-6}, of the light is inelastically scattered at higher and lower frequency. This inelastic scattering is the Raman effect. The frequency shift arises from an energy exchange process in which an incident photon of frequency ν_o is absorbed by a molecule which emits another photon of modified frequency, ν. The process involves a momentary distortion of the electrons distributed about a molecule by an incoming photon, followed by reemission of modified radiation as the molecule relaxes to its ground electronic state. In its distorted form, the molecule is said to have an induced (or temporary) dipole moment. The oscillation of this induced dipole moment in the presence of the incident electric field is the prerequisite for Raman activity.

The frequency of oscillation depends on the facility with which the incident electric field can periodically disturb the electron distribution. This facility is called the polarizability. It is a measure of the ease with which electrons can be displaced by the action of the applied electric field to induce an electric dipole. It is specific to each type of molecule. The polarizability of a molecule changes as a function of internuclear separation and is usually direction dependent. It may be generally regarded as the sum of contributions from individual bond polarizabilities. Bond stretching increases the polarizability of that bond and compression causes the polarizability to decrease. If a particular vibrational motion i causes the molecular polarizability to change with a frequency ν_i, then the induced dipole moment will change with the frequencies ν_0, $\nu_0-\nu_i$, and $\nu_0+\nu_i$ and that motion is a Raman active mode. This means that the scattered radiation will consist of frequencies ν_o (called Rayleigh scattering) and $\nu_o \pm \nu_i$ (called

Raman scattering). Hence the frequency at which the polarizability is changing is equal to the frequency of that particular vibration and is called the Raman frequency shift.

Thus in Raman spectra, the frequency of interest is the difference between the frequency of a particular vibrational mode and the incident radiation. This is the practical advantage of Raman spectroscopy in that scattering can be observed independent of the incident radiation, the frequency of which does not have to coincide with a transition frequency of a sample. In practice, the Raman shift is determined from $\nu_R = \nu_o - \nu_i$ which are called *Stokes* lines as opposed to *anti-Stokes* lines $\nu_R = \nu_o + \nu_i$. Stokes lines result when the incident light loses energy to the molecule and anti-Stokes lines result when the light gains energy from the molecule. Although not predicted in the classical description of Raman theory, Stokes lines are more intense than anti-Stokes because the population of molecules in higher vibrational states at ambient temperature such that they can impart energy to the incident radiation is small.

References

AMAT G. and PIMBERT M. (1965) On Fermi resonance in carbon dioxide. *J. Mol. Spectroscopy* **16**, 278-290.

ANDERSON A. J. and BODNAR R. J. (1993) An adaption of the spindle stage for geometric analysis of fluid inclusions. *Am. Min.* **78**, 657-664.

BERTRAN J. F. (1983) Study of the Fermi doublet ν_1-$2\nu_2$ in the Raman spectra of CO_2 in different phases. *Spectrochimica Acta* **39A**, 119-121.

BODNAR R. J., REYNOLDS T. J., and KUEHN C. A. (1985) Fluid inclusion systematics in epithermal systems. In *Geology and Geochemistry of Epithermal Systems* (eds. B. R. BERGER and P. M. BETHKE), *Rev. Econ. Geol.* 2, pp. 73-97.

BODNAR R. J. and STERNER S. M. (1987) Synthetic fluid inclusions. In *Hydrothermal experimental techniques* (eds. G. C. ULMER and H. L. BARNES), pp. 423-457. Wiley.

BOTTINGA Y. and RICHET P. (1980) High pressure and temperature equation of state and calculation of the thermodynamic properties of gaseous carbon dioxide. *Am. J. Sci.* **281**, 615-660.

BURKE E. A. J. (1994) Raman microspectrometry of fluid inclusions: The daily practice. In *Fluid Inclusions in Minerals: Methods and Applications* (eds. B. DE VIVO and M. L.

FREZZOTTI), *Short Course on Fluid Inclusions, International Mineralogical Association*, pp. 25-44.

BURNS K., ADAMS K. B., and LONGWELL J. (1950) Interference measurements in the spectra of neon and natural mercury. *J. Opt. Soc. Am.* **40**, 339-334.

CHANDRASEKHARAN V. and GARRABOS Y. (1988) Density effect on the Fermi resonance in the high-density phases of CO_2. In *Proceedings of the Eleventh International Conference on Raman Spectroscopy* (eds. R. J. H. CLARK and D. A. LONG), pp. 489-490. Wiley.

CHOU I-M., PASTERIS J. D., and SEITZ, J. C. (1990) High-density volatiles in the system C-O-H-N for the calibration of a laser Raman microprobe. *Geochim. Cosmochim. Acta* **54**, 535-544.

COLLINS P. L. F. (1979) Gas hydrates in CO_2-bearing fluid inclusions and the use of freezing data for estimation of salinity. *Econ. Geol.* **74**, 1435-1444.

DIAMOND L. M. (1994a) Salinity of multivolatile fluid inclusions determined from clathrate hydrate stability. *Geochim. Cosmochim. Acta* **58**, 19-41.

DIAMOND L. M. (1994b) Introduction to phase relations of CO_2-H_2O fluid inclusions. In *Fluid Inclusions in Minerals: Methods and Applications* (eds. B. DE VIVO and M. L. FREZZOTTI), *Short Course on Fluid Inclusions, International Mineralogical Association*, pp. 25-44.

DICKINSON R. G., DILLON R. T., and RASETTI F. (1929) Raman spectra of polyatomic gases. *Phys. Rev.* **34**, 582-589.

DUSCHEK W., KLEINRAHM R., and WAGNER W. (1990) Measurement and correlation of the (pressure, density, temperature) relation of carbon dioxide. I. The homogeneous gas and liquid regions in the temperature range from 217 K to 340 K at pressures up to 9 MPa. *J. Chem. Thermodynamics* **22**, 827-840.

FERMI E. (1931) Uber den Ramaneffekt des kohlendioxyds. *Z. Physik* **71**, 250-259.

GARRABOS Y., TUFEU R., LE NEINDRE B., ZALCZER G., and BEYSENS D. (1980) Rayleigh and raman scattering near the critical point of carbon dioxide. *J. Chem. Phys.* **72**, 4637-4651.

GARRABOS Y., CHANDRASEKHARAN V., ECHARGUI M. A., and MARSAULT-HERAIL F. (1989a) Density effect on the Raman Fermi resonance in the fluid phases of CO_2. *Chem. Phys. Lett.* **160**, 250-256.

GARRABOS Y., ECHARGUI M. A., and MARSAULT-HERAIL F. (1989b) Comparison between the density effects on the levels of the Raman spectra of the Fermi resonance doublet of the $^{12}C^{16}O_2$ and $^{13}C^{16}O_2$ molecules. *J. Chem. Phys.* **91**, 5869-5881.

GORDON H. R. and MCCUBBIN T. K. (1966) The 2.8-micron bands of CO_2. *J. Mol. Spectroscopy* **19**, 137-154.

HEDENQUIST J. W. and HENLEY R. W. (1985) The importance of CO_2 on freezing point measurements of fluid inclusions: Evidence from active geothermal systems and implications for epithermal ore deposition. *Econ. Geol.* **80**, 1379-1406.

HERZBERG G. (1945) *Infrared and Raman Spectra of Polyatomic Molecules, Molecular Spectra and Molecular Structure II.*, D. Van Nostrand Co., Inc., 632 p.

HOWARD-LOCK H. E. and STOICHEFF B. P. (1971) Raman intensity measurements of the Fermi diad ν_1, $2\nu_2$ in $^{12}CO_2$ and $^{13}CO_2$. *J. Mol. Spectroscopy* **37**, 321-326.

LARSON S. D. (1955) Phase studies of the two-component carbon dioxide-water system involving the carbon dioxide hydrate. Ph.D. dissertation, Univ. Michigan.

LONG D. A. (1977) *Raman Spectroscopy.*, McGraw-Hill, 276 p.

LOWRY H. H. and ERICKSON W. R. (1927) The densities of coexisting liquid and gaseous carbon dioxide and the solubility of water in liquid carbon dioxide. *J. Am. Chem. Soc.* **49**, 2729-2934.

MALYJ M. and GRIFFITHS J. E. (1983) Stokes/Anti-Stokes Raman vibrational temperatures: Reference materials, standard lamps, and spectrophotometric calibrations. *Appl. Spectroscopy* **37**, 315-333.

MAY A. D., DEGEN V., STRYLAND J. C., and WELSH H. L. (1961) The Raman effect in gaseous hydrogen at high pressure. *Can. J. Phys.* **39**, 1769-1783.

PASTERIS J. D., WOPENKA B., and SEITZ J. C. (1988) Practical aspects of quantitative laser Raman microprobe spectroscopy for the study of fluid inclusions. *Geochim. Cosmochim. Acta* **52**, 979-988.

ROEDDER E. (1972) Composition of fluid inclusions. In *Data of Geochemistry, 6th ed., U. S. Geol. Survey Prof. Paper 440-JJ* (ed. M. FLEISCHER), 164 p.

ROEDDER E. (1984) *Fluid Inclusions, Rev. Mineral.* 12.

SASADA M. (1985) CO_2-bearing fluid inclusions from geothermal fields. In *Transactions of the Geothermal Resources Council* 9, part 1, pp. 351-356.

SEITZ J. C., PASTERIS J. D., and MORGAN G. B. (1993) Quantitative analysis of mixed volatile fluids by Raman microprobe spectroscopy: A cautionary note on spectral resolution and peak shape. *Appl. Spectroscopy* **47**, 816-820.

STERNER S. M. and BODNAR R. J. (1991) Synthetic fluid inclusions. X: Experimental determination of P-V-T-X properties in the CO_2-H_2O system to 6 Kb and 700°C. *Am. J. Sci.* **291**, 1-54.

ULRICH M. R. and BODNAR R. J. (1988) Systematics of stretching of fluid inclusions II: Barite at 1 atm confining pressure. *Econ. Geol.* **83**, 1037-1046.

WANG C. H. and WRIGHT R. B. (1973) Raman studies of the effect of density on the Fermi resonance in CO_2. *Chem Phys. Lett.* **23,** 241-246.

WIENECKE P., FINSTERHOLZL H., SCHROTTER H. W., and BRANDMULLER J. (1986) Raman spectra of carbon dioxide and its isotopic variants in the Fermi resonance region. Part IV: Temperature dependence on Q-branch intensities from 300 K to 650 K. *Appl. Spectroscopy* **40**, 70-76.

WINEFORDNER J. D. and RUTLEDGE M. (1985) Comparison of calculated detection limits in molecular absorption, molecular luminescence, Raman, molecular ionization, and photothermal spectrometry. *Appl. Spectroscopy* **39**, 377-391.

WOPENKA B. and PASTERIS J. D. (1987) Raman intensities and detection limits of geochemically relevant gas mixtures for a laser Raman microprobe. *Anal. Chem.* **59**, 2165-2170.

WRIGHT R. B. and WANG C. H. (1973) Density effect on the Fermi resonance in gaseous CO_2 by Raman scattering. *J. Chem. Phys.* **58**, 2893-2895.

WRIGHT R. B. and WANG C. H. (1974) Effect of density on the Raman scattering of molecular fluids. II. Study of intermolecular interaction in CO_2. *J. Chem. Phys.* **61**, 2707-2710.

Vita

Kevin Rosso was born on October 8, 1968 in Lynwood, Los Angeles County, California. He spent most of his youth in the city of Stanton which is in Orange County in southern California. Upon graduation from Whittier Christian High School in 1986, his family moved to Brea, California where he began attending California State Polytechnic University at Pomona. His initial interests were in architecture but he later found greater satisfaction from the field of geology. He earned his Bachelor of Science degree in Geological Sciences and was accepted into the graduate program at Virginia Polytechnic Institute and State University in the spring of 1992. He completed a Masters of Science in Geological Sciences in the fall of 1994 and subsequently began working towards a Ph.D. in the field of mineral surface geochemistry.